remote sensing

MDPI

Article

Polarimetric Radar Signatures and Performance of Various Radar Rainfall Estimators during an Extreme Precipitation Event over the Thousand-Island Lake Area in Eastern China

Yabin Gou [1,2], Haonan Chen [3,4] and Jiafeng Zheng [5,*]

1 Hangzhou Meteorological Bureau, Hangzhou 310051, China; 2017011201@cuit.edu.cn
2 Zhejiang Institute of Meteorological Sciences, Hangzhou 321000, China
3 NOAA/Earth System Research Laboratory, Boulder, CO 80305, USA; haonan.chen@noaa.gov
4 Cooperative Institute for Research in the Atmosphere, Fort Collins, CO 80523, USA
5 Plateau Atmosphere and Environment Key Laboratory of Sichuan Province, School of Atmospheric Sciences, Chengdu University of Information Technology, Chengdu 610225, China
* Correspondence: zjf1988@cuit.edu.cn; Tel.: +86-137-3083-2538

Received: 19 August 2019; Accepted: 6 October 2019; Published: 9 October 2019

Abstract: Polarimetric radar provides more choices and advantages for quantitative precipitation estimation (QPE) than single-polarization radar. Utilizing the C-band polarimetric radar in Hangzhou, China, six radar QPE estimators based on the horizontal reflectivity (Z_H), specific attenuation (A_H), specific differential phase (K_{DP}), and double parameters that further integrate the differential reflectivity (Z_{DR}), namely, R(Z_H, Z_{DR}), R(K_{DP}, Z_{DR}), and R(A_H, Z_{DR}), are investigated for an extreme precipitation event that occurred in Eastern China on 1 June 2016. These radar QPE estimators are respectively evaluated and compared with a local rain gauge network and drop size distribution data observed by two disdrometers. The results show that (i) although R(A_H, Z_{DR}) underestimates in the light rain scenario, it performs the best among all radar QPE estimators according to the normalized mean error; (ii) the optimal radar rainfall relationship and consistency between radar measurements aloft and their surface counterparts are both required to obtain accurate rainfall estimates close to the ground. The contamination from melting layer on A_H and K_{DP} can make $R(A_H)$, $R(A_H, Z_{DR})$, $R(K_{DP})$, and $R(K_{DP}, Z_{DR})$ less effective than $R(Z_H)$ and $R(Z_H,Z_{DR})$. Instead, adjustments of the α coefficient can partly reduce such impact and hence render a superior A_H–based rainfall estimator; (iii) each radar QPE estimator may outperform others during some time intervals featured by particular rainfall characteristics, but they all tend to underestimate rainfall if radar fails to capture the rapid development of rainstorms.

Keywords: polarimetric radar; attenuation correction; extreme weather; eastern China; quantitative precipitation estimation (QPE)

1. Introduction

Polarimetric radar measurements, including horizontal reflectivity (Z_H), radial velocity (Vr), differential reflectivity (Z_{DR}), the copolar correlation coefficient (ρ_{HV}), the differential propagation phase (Φ_{DP}), and the specific differential phase (K_{DP}), have the potential to be used in the areas of severe weather/tornado warnings, cloud microphysics, and rainfall estimation/forecasting, which are all important modern meteorological and hydrological applications [1–9]. Recently, all the operational weather radars in the U.S. (i.e., Next-Generation Radar—NEXRAD), UK, and Ireland have been upgraded with dual-polarization capability [10], which can transmit/receive horizontal

and vertical radar waves simultaneously, and weather radars in many other European countries are almost at full dual-polarization capability. Some weather radar sites in China have also been upgraded to dual-polarization capability to replace the original single-polarization weather radars. In addition, some experimental or operational X-band polarimetric radar networks have been deployed near metropolitan urban areas to monitor small-scale severe weather systems [2–5], which makes the synthesis of polarimetric radars for severe weather diagnosis, warning, and decision-making operations more important than ever. Among these operations, radar quantitative precipitation estimation (QPE) plays an indispensable role, and it is a challenging task to obtain accurate structure of the rain rate (R) field [9,11] for flood or mudslide warnings in mountainous areas and waterlogging prevention, especially in densely populated urban areas [3–5].

Conventional single-polarization radar QPE procedures use Z_H as the main source for rainfall field retrieval. For example, the national multi-radar quantitative precipitation estimation system in the United States and Canada [12] is based on Z_H, which has been recently refined by incorporating different Z–R relationships that vary based on climatology. Since single-polarization weather radar is still prevalent in China, and the gauge network in Eastern China is nearly ten times denser than that in the U.S., radar-gauge fitted Z–R relationships have also been incrementally improved recently, mainly by utilizing the gauge-feedback mechanism [13]. However, on one hand, Z_H is inevitably affected by data quality issues, such as miscalibration, attenuation, and partial beam blockage (PBB), and wet radome effects, etc. These negative effects can be significant, especially for X- and C-band radar, and are hard to completely mitigate for single-polarization radar [14–16]. On the other hand, the Z–R relationships based on the feedback mechanism assume the gauge measurements to be the "truth". Radar-estimated rainfall has to approximate the gauge measurements, and any uncertainty in gauge measurements may degrade the practical performance of fitted Z–R relationships.

With more and more weather radar systems being updated with dual-polarization capability, many researchers have been focusing on improving the performances of radar QPE algorithms based on independent or composite utilization of polarimetric variables, which provides a complementary alternative to conventional radar QPE algorithms. Among these, K_{DP} is preferable for many researchers and there are at least three reasons why K_{DP} is more attractive for rainfall estimation. First, K_{DP} is proportional to a moment of the particle size distribution (PSD) closer to that of the rain rate. The rain rate is proportional to approximately the 3.67^{th} moment of the PSD, while K_{DP} is proportional to the ~4.24^{th} moment [17] and Z_H is proportional to the ~6^{th} moment. Therefore, K_{DP} is much less sensitive to changes in the concentration of the largest drops that do not contribute much to the total rainfall. In addition, K_{DP} is immune to isotropic scatterers and is frequently assumed to be near-zero for tumbling hail. Last, K_{DP} is characterized by immunity to miscalibration, attenuation, and PBB and wet radome effects; conversely, these issues may degrade the quality of Z_H measurements [18].

Considering that raindrop shape can be indirectly deduced from Z_{DR}, the double-parameter radar QPE algorithm based on Z_H and Z_{DR}, namely, $R(Z_H, Z_{DR})$, is a better choice than $R(Z_H)$, assuming that Z_H and Z_{DR} are both well calibrated and attenuation-corrected [1,18]. For a similar reason, $R(K_{DP}, Z_{DR})$ was established as another double-parameter radar QPE estimator through combining Z_{DR} with K_{DP}; however, not all reports have concluded that $R(K_{DP}, Z_{DR})$ can outperform $R(K_{DP})$, especially at X-band [15,19,20]. Triple-parameter radar QPE estimators, such as $R(Z_H, Z_{DR}, K_{DP})$, have also been proposed at X-band [21], which can further incorporate the altitude of radar measurements to account for the drop fall velocity changes caused by changes in the density of ambient air [22]. However, the triple-parameter radar QPE estimator is less widely used, because an increased number of radar variables may introduce more uncertainty. The specific attenuation (A_H) is insensitivive to raindrop size distribution (DSD) variability, and recent investigations show that $R(A_H)$ performs better than $R(Z_H)$ at X-band and S-band [23–25]. In addition, A_H can also be joined with Z_{DR} to form a double-parameter estimator, denoted by $R(A_H, Z_{DR})$, which was declared to be less affected by the biases due to the assumed raindrop axial ratio [26,27] at the X-band, but this algorithm has never been examined at the C-band radar.

The novel contributions of this paper are as follows: (i) We develop and test a new $R(A_H,Z_{DR})$ estimator for a C-band polarimetric (CPOL) radar for the first time, which utilizes the improved self-consistent attenuation correction method (i.e., the ZPHI approach) proposed by Bringi et al. [28] through the incorporation of more microphysical constraints in the correction process of Z_H and Z_{DR} [29,30]. (ii) We also intercompare different radar rainfall estimators to address their advantages and disadvantages, utilizing the first high-quality and high-resolution (i.e., 125 m range resolution and 0.46 deg azimuthal resolution) CPOL radar deployed in Hangzhou, China and rainfall recordings of the highly dense gauge network around Hangzhou. (iii) We develop optimal radar QPE parameters for monsoon rainfall using the regional DSD dataset during a serious waterlogging event around the Thousand-Island Lake (TIL) area in Eastern China. The rest of this manuscript is organized as follows: Section 2 introduces the dataset used in this study and the data processing methods involved; Section 3 examines the comparison results of different radar QPE algorithms; and Section 4 summarizes and concludes this study.

2. Study Domain, Dataset, and Rainfall Methodology

2.1. Study Area and Hardware Configuration

The CPOL radar in Hangzhou is situated on a high mountain top (1512 m above sea level) around the complex mountainous area in eastern China, as depicted in Figure 1a. The TIL area is located within 100 km of the CPOL radar site with the altitude of radar beams 1.6–2.1 km above-ground-level (and no beam blockage over the TIL area). It is an important artificial lake which covers an area of 580 km^2 under normal water levels, and it was constructed mainly for the Xin-An River hydropower station. The study domain shown in the rectangle in Figure 1a covers the southern area of Chun An (CA) town and the western area of Jiang De (JD) town of Hangzhou, and the mountainous terrain that surrounds the north and south areas of TIL. In addition, TIL is situated just at the upper stream of the Qiantang River, along which are densely populated areas; therefore, hydrologic monitoring around the TIL area is very important, especially in the summer monsoon season.

The unique topography around the TIL area makes the CPOL radar an indispensable seamless surveillance device for severe rainfall monitoring and nowcasting operations, because the other radar sites are either far from this area or seriously blocked by the mountainous terrain. The CPOL radar is mainly configured with simultaneous horizontal and vertical polarization modes for its routine daily operations. The elevation angles of its volume coverage pattern (VCP) have been set as 0.0°, 0.5°, 1.5°, 2.5°, 3.5°, 4.5°, 6.0°, 7.5°, and 9.0° since September 2015 and one VCP scan can be finished in about six minutes. The azimuthal radial resolution of three lowest three VCP sweeps are configured as 0.46°; the others are configured as 0.95°. In addition, the range gate resolution of the CPOL radar is configured as 125 m at all elevations. The measured Ψ_{DP}, Z_H, Z_{DR}, ρ_{HV}, and radial velocity are all archived into a ".bz2" package in the radar data acquisition (RDA) system for posterior product generation.

Two second-generation Particle Size and Velocity (Parsivel^2) disdrometers, which can provide simultaneous measurements of the particle size and falling velocity information of raindrops with a sampling resolution of one minute, were deployed at the national meteorological stations at CA and JD towns, respectively (see the bold "+" in Figure 1a,b). They are maintained routinely to ensure the data quality of DSD measurements, which are important surface observation sources that are used to simulate dual-polarization radar measurements and to investigate regional rainfall characteristics. In addition, 786 tipping-bucket gauge stations (see small "+" in Figure 1b) were deployed within range of 100 km from the CPOL radar. The temporal resolution of the rain gauges is also specified as one minute. The gauge observations without any interruptions are used for the verification of radar rainfall estimates, and if any ratios between six radar hourly estimates and gauge hourly measurements exceed 5, the gauge measurements are suspected to be false reports and will be abandoned and not used for the validation aim. This simple quality control procedure can eliminate a small portion of significantly biased gauge measurements but keep most large rainfall recordings.

A severe rainfall event on 01 June 2016 caused a large area of JD town to suffer from a serious waterlogging disaster. Several people were not evacuated immediately and were trapped in the disaster zone. The meteorological stations situated in the severe rainfall center area, including Jia Ziling (JZL), Shi Lin (SL), Qian Daohu (QDH), Xi Hua (XH), Shou Chang (SC), Geng Lou (GL), Zhi Yan (ZY), and Gan Xi (GX), are all marked with small "+" symbols in Figure 1c. The pictures in Figure 1c depict the waterlogging scenes that show a large area of submerged farmland around this area and the local emergency managers were working near GL station aiming to rescue the trapped people in the village near GL station.

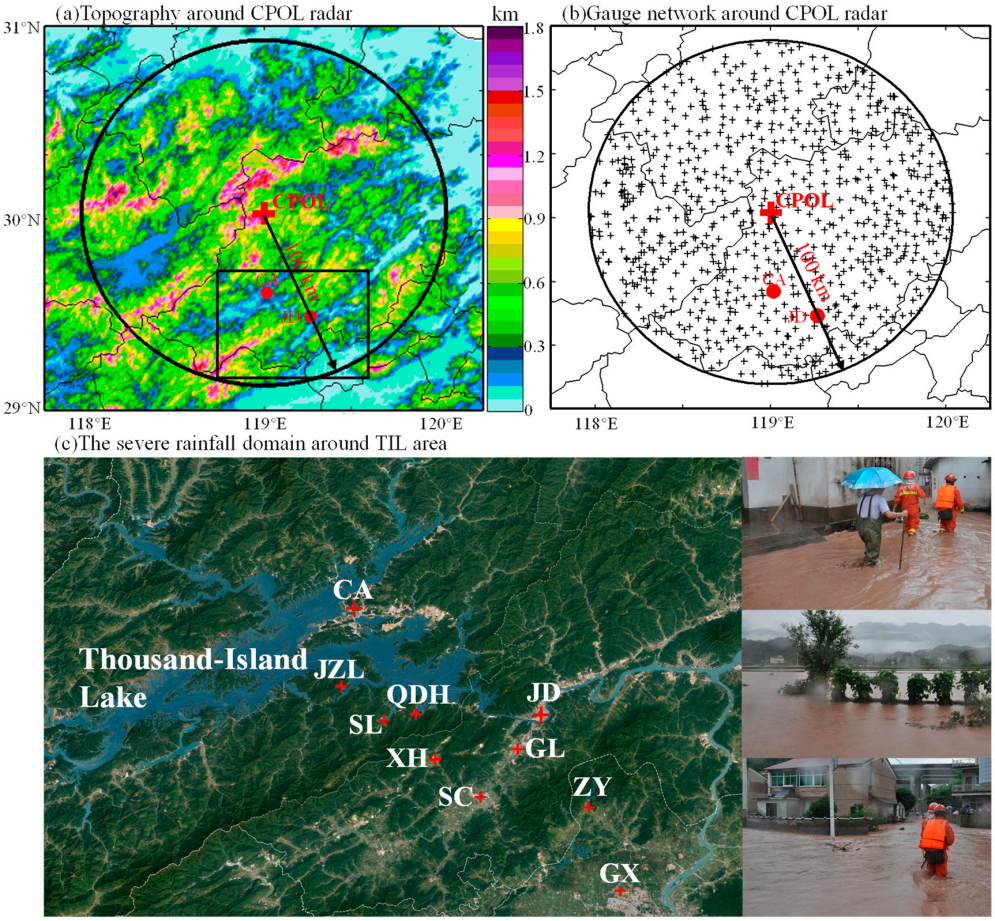

Figure 1. (**a**) Topography around the C-band polarimetric (CPOL) radar (red "+"); (**b**) gauge network (black "+") within 100 km of the CPOL radar; the Parsivel^2 disdrometers deployed at CA and JD are marked with red dots on (**a**) and (**b**); (**c**) the severe rainfall domain (i.e., the rectangle in (**a**)) around the TIL area and sample photos taken during the 1 June 2016 event. Eight stations with the largest 3-h rainfall quantities and two disdrometer stations are marked with a red "+" in (**c**).

2.2. Radar Data Processing

Radar quality control procedures imposed on polarimetric radar variables were successively implemented. Several key issues within the procedure include the following processing steps:

(i) Ground clutter (GC) mitigation.

The clutter mitigation decision (CMD) algorithm proposed by Hubbert et al. [31] was utilized and integrated into the radar data acquisition (RDA) software. The CMD algorithm incorporates clutter phase alignment that was extracted from the radar I and Q (in-phase and quadrature-phase) data, the spatial texture of Z_H, the spin-change of Z_H, which was defined by Steiner and Smith (2002) [32] to measure how often the reflectivity gradient changes sign along the radar radial, and the standard deviation of Z_{DR} and Ψ_{DP} as the input parameters of a fuzzy logic scheme to identify the GC signals.

Radar measurements were instantaneously filtered in the scanning process to eliminate the GC signal contamination. The statistics of the Z_H measurements before and after the clutter filtering during June 2016 at an elevation 0° show that the maximum number (N_{max}) of pixels with $Z_H > 0$ dBZ in the range of 180 km of the CPOL radar was 6981. The observation number (N_{obs}) of each pixel was normalized by dividing N_{max} to derive the relative frequency (Freq.%) of these pixels, and the results are depicted in Figure 2. The GC pixels with a high probability of occurrence in Figure 2a are effectively eliminated in Figure 2b. In addition, the pixels in Figure 2b are still spatially continuous and smooth, which indicates the effectiveness of the CMD algorithm.

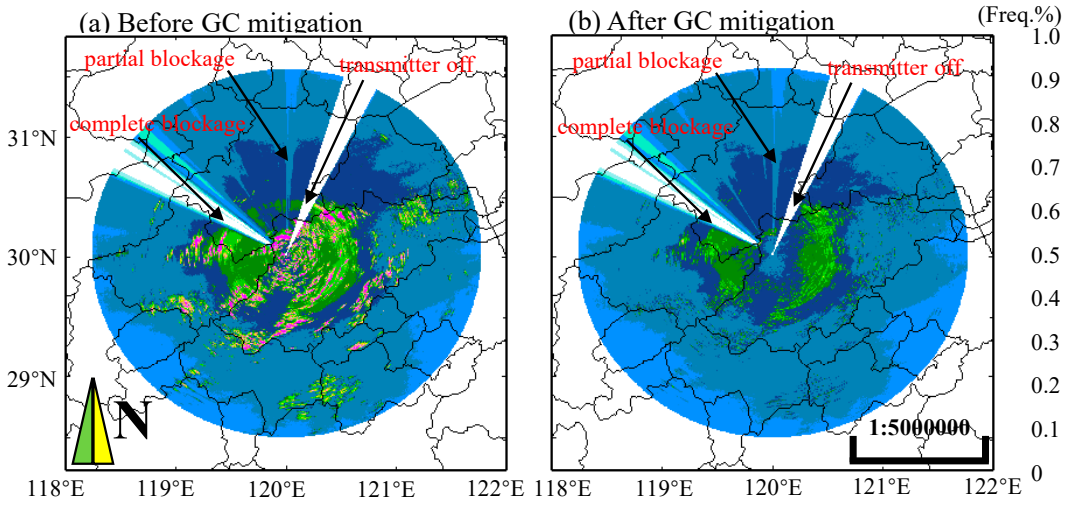

Figure 2. The relative frequency (Freq.%) of pixels with $Z_H > 20$ dBZ within range of 180 km from the CPOL radar: (**a**) Before GC mitigation; (**b**) After GC mitigation.

(ii) Ψ_{DP} Processing.

The spike signal, which refers to the large and sharp increase of Ψ_{DP} along the range profile, was first suppressed by using the average of its two aligned range gates without any large changes with respect to the aligned four range gates. Then, a nine-gate average operation was used to smooth the Ψ_{DP} range profile. According to the monotonous increasing characteristics of the Ψ_{DP} range profile, a Ψ_{DP} dealiasing procedure was then executed if the measured Ψ_{DP} exceeded 360°, and the standard deviation of Ψ_{DP} derived from nine consecutive range gates was used in this process [33]. The iterative filtering method [34,35] was used to filter the backscatter differential phase and to obtain a high quality Φ_{DP} ($\Phi_{DP}^{filtered}$) range profile. Finally, the initial phase of Φ_{DP} was determined using the linear regression method and removed from the Φ_{DP} range profile. The Φ_{DP} range profile was then utilized to estimate K_{DP} through the linear fitting approach [33] and the posterior attenuation correction of Z_H.

(iii) Calibration and attenuation correction.

For practical implementation, the ZPHI method proposed by Bringi et al. [28], which is demonstrated in Equations (1a)–(1f), was imposed with three constraints: A non-negative constraint on A_H estimation, a ρ_{HV} constraint on the range gates partitioning process, and a convergence constraint to check whether the difference between Φ_{DP} and reconstructed Φ_{DP}^{rec} in Equation (1e) of every range interval was minimized [29]. It was implemented in every partitioned range interval $[r_0, r_m]$ along each radial profile to estimate the specific attenuation (A_H) according to Equations (1a)–(1d) by assuming a constant parameter b (0.78) [28]. Then, the optimal parameters of α_{opt} were searched for in [0.03, 0.18] to minimize the difference between Φ_{DP} and the reconstructed Φ_{DP}^{rec} in Equation (1e) in each partitioned range interval. Finally, the measured Z_H (Z_H^M) was corrected by Equation (1f) as Z_H^C utilizing the optimally estimated A_H. Z_H^C and A_H were respectively used in $R(Z_H)$ and $R(A_H)$.

$$A_{\mathrm{H}}(r) = \frac{\left[Z_{\mathrm{H}}^{\mathrm{M}}\right]^{b}\left[10^{0.1b\alpha\Delta\Phi(r_0,r_m)} - 1\right]}{I(r_0,r_m) + \left[10^{0.1b\alpha\Delta\Phi(r_0,r_m)} - 1\right]I(r,r_m)} \tag{1a}$$

$$\Delta\Phi_{\mathrm{DP}}(r_0,r_{\mathrm{m}}) = \Phi_{\mathrm{DP}}(r_{\mathrm{m}}) - \Phi_{\mathrm{DP}}(r_0) \tag{1b}$$

$$I(r_0,r_m) = 0.46b\int_{r_0}^{r_m}\left[Z_{\mathrm{H}}^{\mathrm{M}}(r)\right]^{b}dr \tag{1c}$$

$$I(r,r_m) = 0.46b\int_{r}^{r_m}\left[Z_{\mathrm{H}}^{\mathrm{M}}(r)\right]^{b}dr \tag{1d}$$

$$\Phi_{\mathrm{DP}}^{\mathrm{rec}}(r_0,r_m) = \int_{r_0}^{r_m}\frac{A_{\mathrm{H}}(s,\alpha)}{\alpha}ds \tag{1e}$$

$$Z_{\mathrm{H}}^{\mathrm{C}}(r) = Z_{\mathrm{H}}^{\mathrm{M}}(r) + 2\int_{0}^{r}A_{\mathrm{H}}(s,\alpha)ds. \tag{1f}$$

(v) Calibration and attenuation correction of Z_{DR}.

The "birdbath" scan method is routinely carried out for Z_{DR} calibration before the upcoming monsoon season, which is usually performed through vertically pointing observations (elevation of 90°) in a full azimuthal rotation [1]. The Z_{DR} offset can be obtained with respect to the nearly zero values of Z_{DR} in the light rain scenarios, and then this offset is fed back to the RDA system to make sure there is a low Z_{DR} bias. Moreover, an event-derived exponential Z_{DR}–Z_{H} relationship (see the black line on Figure 3a) is shown by Equation (2a). This was derived through the standard weighted least-squares nonlinear fitting method based on the DSD dataset collected during the period 0000–2359 UTC on 1 June 2016. Therein, Z_{H}, Z_{DR}, K_{DP}, and A_{H} were simulated by the T-matrix method, assuming the raindrop aspect ratio presented in Brandes et al. [36], at a temperature of 20 °C.

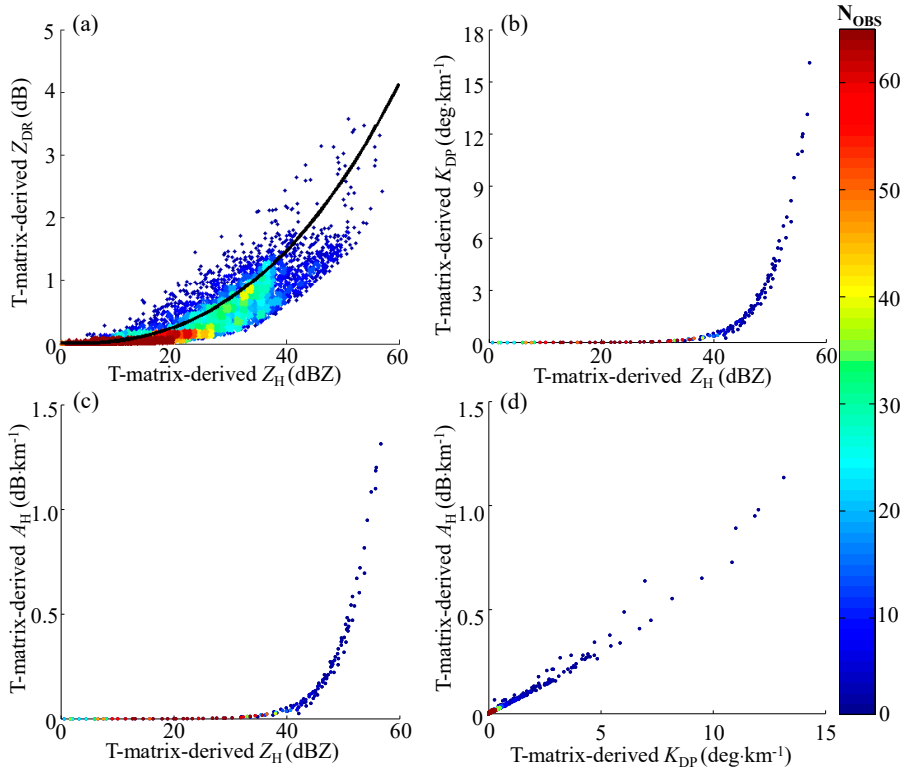

Figure 3. Scattergram of radar variables simulated using the DSD dataset collected on 0000–2359 UTC on 01 June 2016: (**a**) Z_{DR} vs. Z_{H}; (**b**) K_{DP} vs. Z_{H}, (**c**) A_{H} vs. Z_{H}, and (**d**) A_{H} vs. K_{DP}. The black curve in (a) represents the Z_{DR}–Z_{H} relationship in Equation (2a).

The differential attenuation factor (A_{DP}) in Equation (2b) was derived according to the optimal β, which was obtained through minimizing the differences between the estimated Z_{DR} in Equation (2a) and the Z_{DR} guessed by the potential A_{DP} in Equations (2b) and (2c) along the whole radial range profile. Finally, the measured Z_{DR} (Z_{DR}^{M}) along the range profile was corrected by Equation (2c) as Z_{DR}^{C}, which was then integrated with Z_H, K_{DP}, and A_H for rainfall estimation.

$$\hat{Z}_{DR}(r) = 1.377 \times 10^{-4} Z_H^C(r)^{2.5005} \tag{2a}$$

$$A_{DP}(r;\beta) = \frac{\beta}{\alpha_{opt}} A_H\left(r;\alpha_{opt}\right) \tag{2b}$$

$$Z_{DR}^C(r;\beta) = Z_{DR}^M(r) + 2\int_0^r A_{DP}(s,\beta)ds \tag{2c}$$

2.3. The Polarimetric Radar Rainfall Estimators

Utilizing the DSD dataset collected during the period 0000–2359 UTC on 1 June 2016 at CA and JD, the event-derived radar rainfall rate relationships based on $R(Z_H)$, $R(K_{DP})$, $R(A_H)$, $R(Z_H, Z_{DR})$, $R(K_{DP}, Z_{DR})$, and $R(A_H, Z_{DR})$ were established using the T-matrix-derived polarimetric variables for the CPOL radar rainfall applications as follows:

$$R(Z_H) = 0.0457 \times Z_H^{0.633} \tag{3a}$$

$$R(Z_H, Z_{DR}) = 0.0039 \times Z_H^{0.916} Z_{DR}^{-1.604} \tag{3b}$$

$$R(K_{DP}) = 23.598 \times K_{DP}^{0.855} \tag{3c}$$

$$R(K_{DP}, Z_{DR}) = 29.436 \times K_{DP}^{0.896} Z_{DR}^{-0.573} \tag{3d}$$

$$R(A_H) = 203.5894 \times A_H^{0.755} \tag{3e}$$

$$R(A_H, Z_{DR}) = 323.1317 \times A_H^{0.945} Z_{DR}^{-1.922} \tag{3f}$$

Both Z_H and Z_{DR} were on a linear scale. These radar rainfall rate relationships were derived using the standard weighted least-squares nonlinear fitting method with the results depicted Figure 4. The single averaged $R(Z_H)$ and $R(K_{DP})$ relationships were utilized rather than the combined radar QPE estimators, with the aim to see the relative superiority of combined polarimetric radar variables. The pixel-to-pixel linear average accumulation scheme was then used to retrieve radar hourly accumulation field for these radar QPE estimators, and they were then evaluated independently by hourly gauge measurements to see their real performances in the severe rainfall event around the TIL area. Rainfall rates estimated from the polarimetric variables calculated from observed DSDs at CA and JD stations were also accumulated hourly to check the quality of the radar-estimated and gauge-measured hourly rainfall series.

3. Results and Discussion

3.1. Description of Synoptic Characteristics

According to the wind directions (bold arrows) depicted in Figure 5a, there was a quasi-stationary front, and sustained moisture convergence led to persistent convection. The Φ_{DP} measurements, which passed through the convective rainstorms in many radial directions, exceeded 100° (Figure 5b), and they were directly responsible for the large K_{DP} values shown in Figure 5e. According to posterior analysis, these rainstorms had high concentrations of moderately-sized raindrops, and they were intrinsically related to the sustained moisture convergence along the quasi-stationary front. Consequently, the rainstorms showed a northwestern distribution along this front, supported by the large-scale environment.

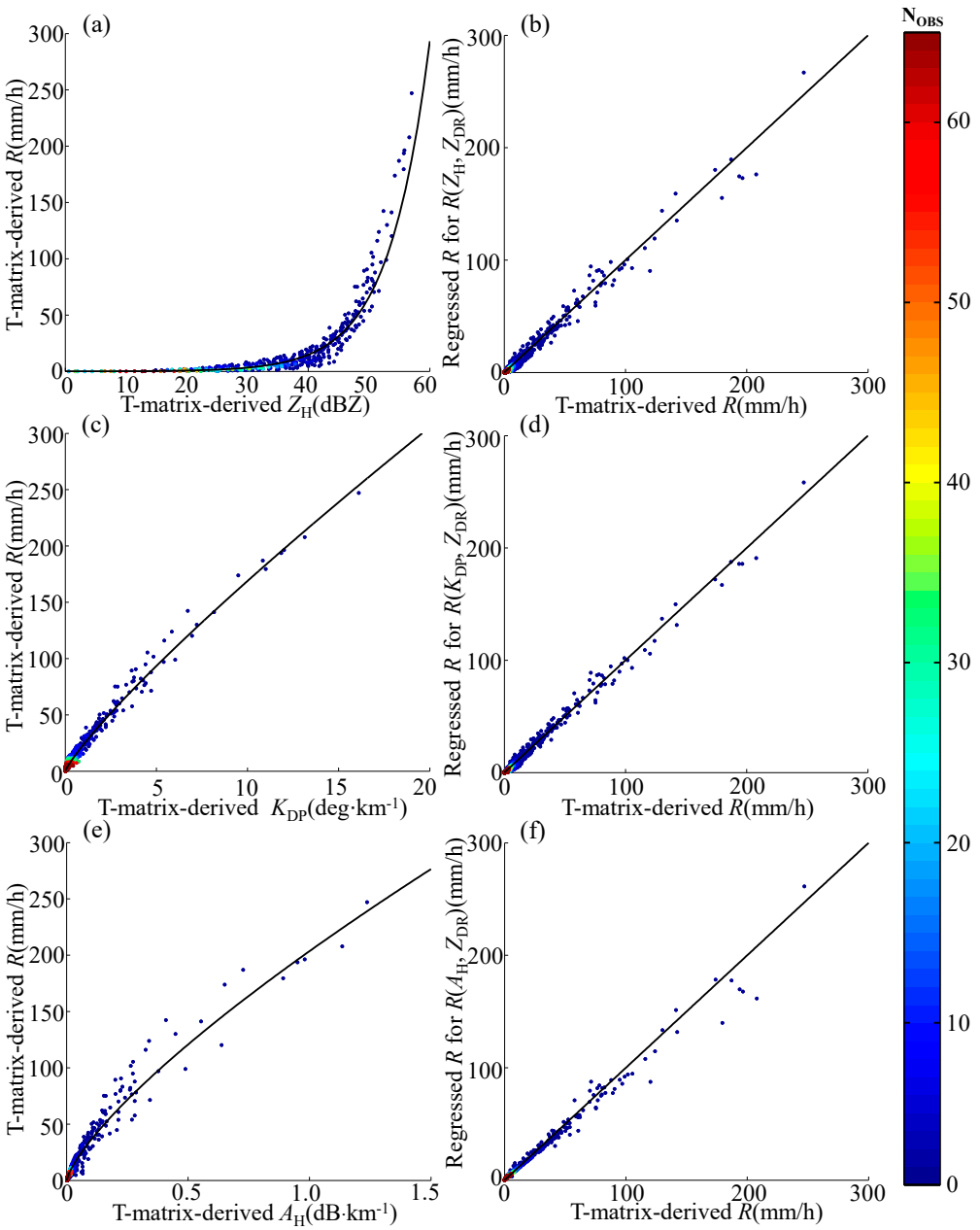

Figure 4. Scattergram between *T*-matrix-derived polarimetric radar variables, as well as estimated/regressed *R* based on the simulated radar variables using the raindrop size distribution (DSD) data collected on 01 June 2016: (**a**) $R(Z_H)$; (**b**) $R(Z_H, Z_{DR})$; (**c**) $R(K_{DP})$; (**d**) $R(K_{DP}, Z_{DR})$; (**e**) $R(A_H)$; (**f**) $R(A_H, Z_{DR})$. The black lines in (a–c) represent Equations (3a), (3c), and (3e), respectively. *T*-matrix-derived *R* stands for *R* calculated directly from the DSD data.

For the posterior analysis, the consistency between Z_H, Z_{DR}, and K_{DP} shown in Figure 5c–e was first verified through the scattergram in Figure 6 to check their quality. The T-matrix-derived Z_H, Z_{DR}, and K_{DP} dataset depicted in Figure 3 was also overlaid on the scattergrams shown in Figure 6 (black dots) for comparison. It can be seen that the scattergram of radar-observed Z_{DR} vs. Z_H presented in Figure 6a agrees well with the T-matrix-derived Z_{DR}–Z_H distributions shown in Figure 3a, and Z_{DR} presented an obvious exponentially increasing tendency as Z_H increased, which coincides with the scattering characteristics of the oblate liquid raindrops. The scattergram of radar-observed K_{DP} and Z_H derived from Figure 5c,e is also consistent with the T-matrix-derived counterparts shown in Figure 3b, and the large Z_H measurements agree well with the large K_{DP} estimates. The consistency between Z_H,

Z_{DR}, and K_{DP} demonstrates that the attenuation correction and calibration of Z_H and Z_{DR} were good. However, radar-observed A_H was not completely consistent with Z_H, as depicted in Figure 6c, and the black T-matrix-derived dots of A_H vs. Z_H just passed through the center area of radar-observed distribution of A_H vs. Z_H. Some radar-observed A_H values were larger than the T-matrix-derived dots of A_H, while others were smaller, particularly when Z_H exceeded 40 dBZ. A_H related to K_{DP} in a linear form as $A_H = \alpha K_{DP}$ with α ranging from 0.03 to 0.18, which can be seen from the ratios between A_H and K_{DP} shown in Figure 6d. That is, the combination of A_H and α together was consistent with attenuation-corrected Z_H measurements. In addition, the range of A_H was relatively small, and the high altitudes (1.6–2.1 km) of the CPOL radar measurements by radar-observed A_H may be very different from their surface counterparts.

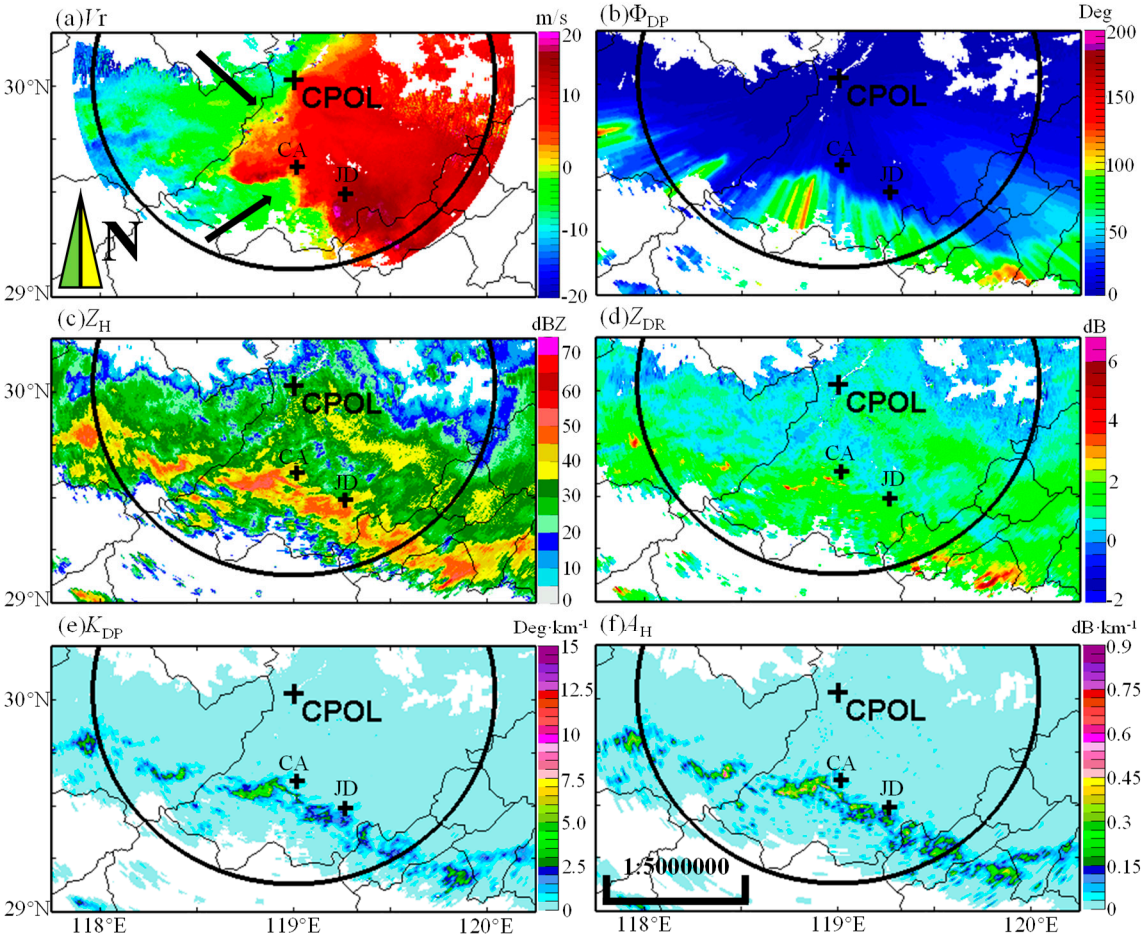

Figure 5. Radar plan position indicator (PPI) scan at an elevation angle of 0° at 0330 UTC on 1 June 2016: (**a**) *V*r; (**b**) Φ_{DP}; (**c**) Z_H; (**d**) Z_{DR}; (**e**) K_{DP} and (**f**) A_H. The relative positions of CA and JD are marked with "+". The bold arrows in (a) describe the northwestern and the southwestern winds.

Some microphysical information about the rainstorms can accordingly be deduced. Assuming the gamma model and neglecting the possible uncertainty induced by parameter *u*, the polynomial relationship between the median volume diameter (D_0) and Z_{DR} and the exponential relationship between the liquid water content (LWC, g·m^{-3}) and K_{DP}, which were fitted using the localized DSD dataset during the monsoon season of Hangzhou [30] and the normalized concentration of raindrops N_w (mm^{-1}·m^{-3}) presented in Ryzhkov et al. (2014) and Testud et al. (2001) [23,37], respectively, can be represented as

$$D_0 = 0.9655 \times {Z_{DR}}^3 - 2.3309 \times {Z_{DR}}^2 + 2.3627 \times Z_{DR} + 0.4252 \quad (4)$$

$$\mathrm{LWC} = 1.0397 \times K_{DP}^{0.9718} \quad (5)$$

$$N_w = \frac{4^4}{\pi \rho_w} \frac{\mathrm{LWC}}{D_m^4} \tag{6}$$

where ρ_w is the water density (1 g·cm^{-3} at 4°C), and D_m (mm) stands for the mean volume diameter of the DSD. It is clearly seen that only a small part of Z_DR measurements in Figures 5d and 6a exceeded 2 dB along the area with positive and negative Vr pairs, which was mainly related to the convective updraft area. Instead, most Z_DR measurements of these rainstorms were featured by Z_H > 20 dBZ and 0.25 dB ≤ Z_DR ≤ 2dB, within which the D_0 of most DSD rarely exceeded 2 mm according to Equation (4), and moderately-sized raindrops with 1 mm ≤ D_0 ≤ 2 mm may be the dominant hydrometeors of these rainstorms. However, the southwestern convergence area shown in Figure 5c was featured by K_DP > 1 deg·km^{-1} with a maximum of 8 deg·km^{-1}, which can also be seen in Figure 6b. Therefore, the LWC within the rainstorm was higher than 1 g·m^{-3} and it increased linearly if K_DP exceeded 1 deg·km^{-1}. The value of D_m in Equation (6) was also expected to be less than 2 mm, and N_w was at least larger than 5000 mm^{-1}m^{-3} if K_DP became larger than 1 deg·km^{-1}, which implied that a high concentration of moderately-sized raindrops within the convective rainstorms was the microphysical reason for this waterlogging disaster. Furthermore, a similar rainfall pattern persisted for more than 3 h over the study area. The radar retrieved rainfall field was indispensable for the decision-making related to this disaster warning.

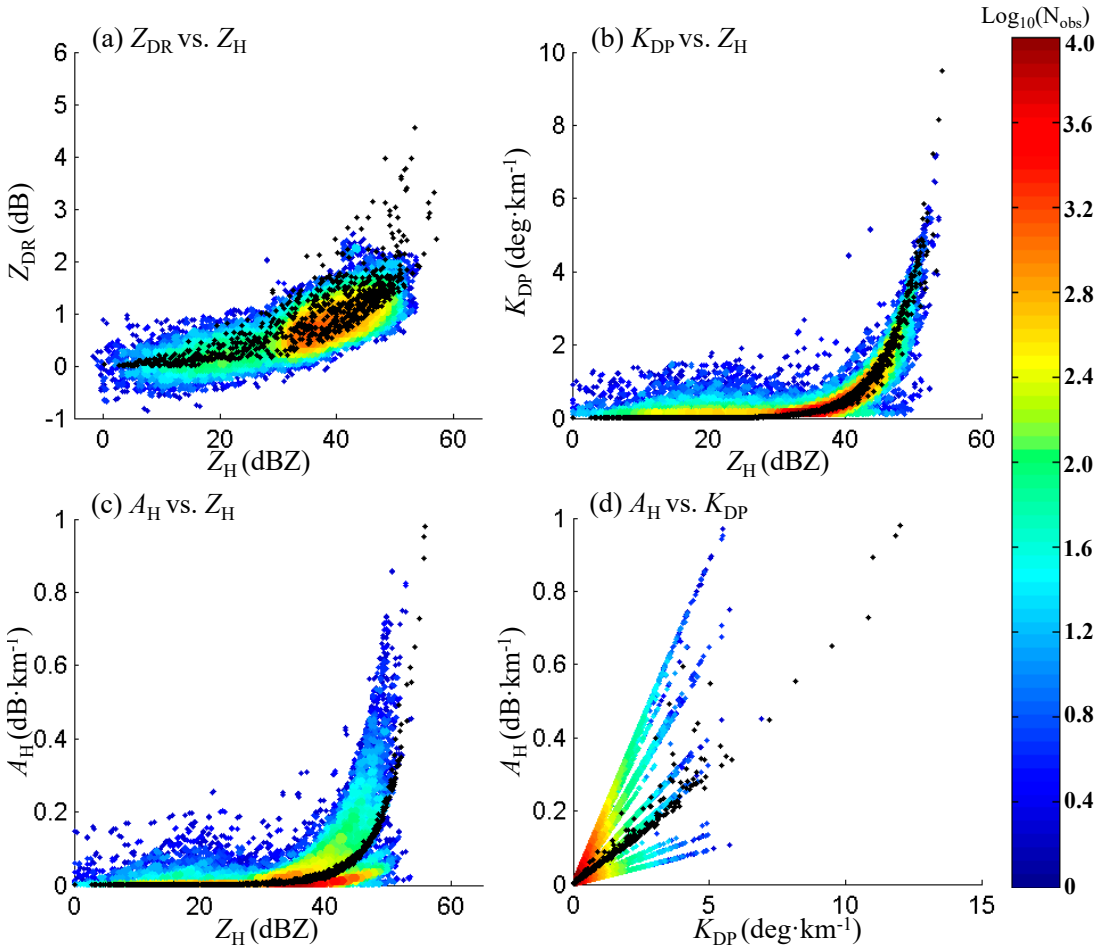

Figure 6. The scattergrams between different radar variables at a scan elevation angle of 0° at 0330 UTC on 1 June 2016: (**a**) Z_DR vs. Z_H (**b**) K_DP vs. Z_H; (**c**) A_H vs. Z_H, (**d**) A_H vs. K_DP. The black dots stand for the simulated radar variables based on the drop size distribution measurements.

3.2. Evaluation Metrics

By utilizing the radar rainfall rate relationships in Equations (3a)–(3f), three single-parameter and three double-parameter radar rainfall fields were retrieved, respectively. The radar hourly estimated rainfall fields within 100 km from the CPOL radar were then compared with hourly gauge rainfall measurements. In addition, rainfall rates calculated from DSD data at CA and JD stations were also aggregated into hourly rainfall measurements for comparison. Three simple statistical scores, including the normalized mean error (E_{NM}), root-mean-square error (E_{RMS}), and correlation coefficient (E_{CC}), were used to evaluate these radar rainfall fields. They were defined as

$$E_{NM} = \frac{\sum_{i=1}^{n}(r_i - g_i)}{\sum_{i=1}^{n} g_i} \times 100\% \tag{7a}$$

$$E_{RMS} = \sqrt{\frac{1}{n}\sum_{i=1}^{n}(r_i - g_i)^2} \tag{7b}$$

$$E_{CC} = \frac{\sum_{i=1}^{n}(r_i - \bar{r})(g_i - \bar{g})}{\sqrt{\sum_{i=1}^{n}(r_i - \bar{r})^2}\sqrt{\sum_{i=1}^{n}(g_i - \bar{g})^2}} \tag{7c}$$

where r_i and g_i are radar-estimated and gauge-observed hourly rainfall accumulations, and $\bar{r}$ and $\bar{g}$ stand for their average values. Smaller $|E_{NM}|$ and E_{RMS} scores and larger E_{CC} scores are associated with superior radar QPE performance.

3.3. Comparison of Different Radar QPE Approaches

By utilizing the rainfall rate relationships in Equations (3a)–(3f), six radar-based 3-h rainfall accumulation fields at 0500 UTC on 1 June 2016 were obtained, as shown in Figure 7. At the same time, the scatter between radar 3-h estimates and gauge 3-h observations are also depicted in Figure 8 to show the relative differences between radar estimates and gauge measurements.

Although the shape of these rainfall fields of $R(Z_H)$ in Figure 7a is similar to that of the others, the score of $R(Z_H)$ in Table 1 shows that $R(Z_H)$ seriously underestimated the rainfall center field. This phenomenon can be clearly seen in Figure 8a, particularly when the gauge 3-h rainfall measurement exceeded 40 mm, and the negative deviation of radar estimates from gauge measurements was more serious with higher rainfall amounts. It can also be seen from Figure 4a that more scatter dots were found above the black curve when Z_H exceeded 50 dBZ, which implies the potential underestimation of $R(Z_H)$ in the rainfall center with higher Z_H measurements. Such uncertainties may result from the absence of separate size information (such as D_0 and D_m) and the concentration information (N_w) of raindrops within the rainstorms, because Z_H was a composite radar moment of these two factors.

Compared with $R(Z_H)$, the scores of $R(Z_H, Z_{DR})$ in Table 1 all improved. Moreover, the radar–gauge data pairs in Figure 8b are more uniformly scattered along the diagonal line (i.e., y = x) than those in Figure 8a. This result indicates that combining the potential raindrop shape information through Z_{DR} was more effective than the single Z_H utilization, as it mitigated this deficiency of Z_H. However, $R(Z_H, Z_{DR})$ is still underestimated since the negative E_{NM} values and more scatter dots distributed below the diagonal line can be observed in Figure 8b.

It is hard to say $R(K_{DP})$ performed better than $R(Z_H)$ from the E_{RMS} comparison in Table 1; however, the scattergram of of $R(Z_H)$ in Figure 8a was more distributed below the diagonal line in Figure 8a than the scattergram of $R(K_{DP})$ in Figure 8c. The latter was more uniformly distributed along the diagnoal line, espically in the range of 0–75 mm, where the scattergram of $R(A_H)$ was more distributed above the diagonal line in Figure 8e. Based on this, $R(K_{DP})$ performed best among single-parameter retrievals. Except for the immunity of K_{DP} to attenuation and wet radome effects, the superiority of $R(K_{DP})$ to the other two single-parameter radar estimates can be attributed to the fact that K_{DP} was more directly and cohesively associated with LWC [38], which is represented by the aforementioned Equation (5).

However, there are more scatter dots distributed above the diagonal line in Figure 8c when the 3-h gauge measurements exceeded 75 mm, which apparently accounts for the overestimation of $R(K_{DP})$ in the rainfall center area.

$R(K_{DP}, Z_{DR})$ further integrated the raindrop shape information through Z_{DR}; however, the scores of $R(K_{DP}, Z_{DR})$ were actually inferior to those of $R(K_{DP})$ shown in Table 1, and the overestimation effect seemed more serious in Figure 8d than that in Figure 8c. This indicates that additional incorporation of Z_{DR} is not effective for $R(K_{DP}, Z_{DR})$, at least in this event, and that the basic equational form of Z_{DR} and K_{DP} in $R(K_{DP}, Z_{DR})$ may account for this phenomenon. It was noticed that $R(K_{DP}, Z_{DR})$ in Schneebeli and Berne [20] assumed the exponent of K_{DP} to be a constant of 1 and just fitted the parameters related to Z_{DR}, which may better utilize the nearly linear relation between K_{DP} and LWC according to Equation (5). In addition, it is better to make the Z_{DR}-related component of $R(K_{DP}, Z_{DR})$ play a micro-adjusting role if the K_{DP}-related component of $R(K_{DP}, Z_{DR})$ can perform at least as well as $R(K_{DP})$. Actually, K_{DP} contains shape information in a less straightforward way than Z_{DR}, since oblateness is always required when radar wave passes through a rainstorm and a spherical particle would have $K_{DP} = 0$ regardless of its size, this partly explains why the addition of Z_{DR} cannot significantly improve $R(K_{DP})$.

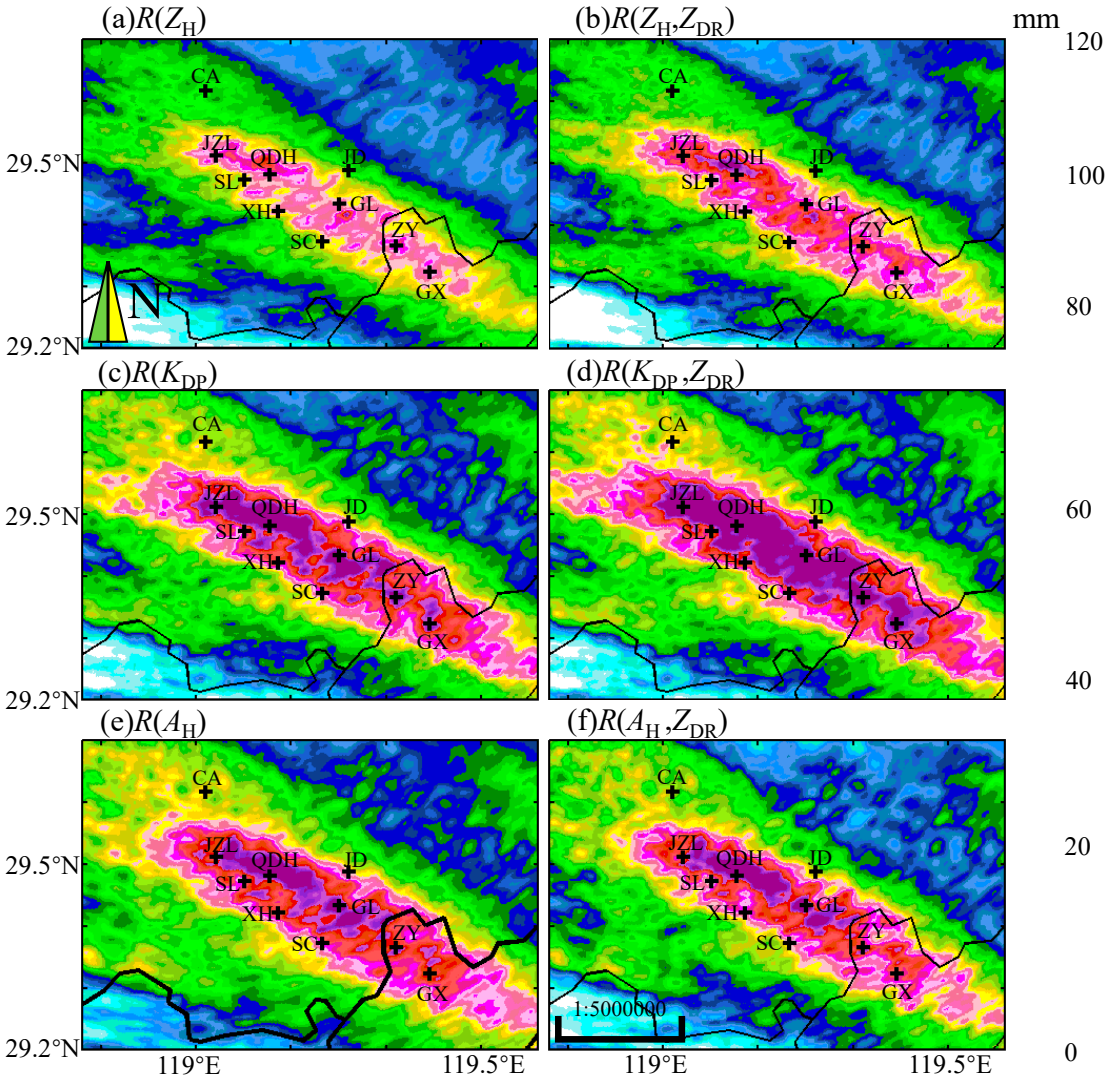

Figure 7. Three hour rainfall accumulation based on six different radar rainfall estimators at 0500 UTC on 1 June 2016: (**a**) $R(Z_H)$; (**b**) $R(Z_H, Z_{DR})$; (**c**) $R(K_{DP})$; (**d**) $R(K_{DP},Z_{DR})$. (**e**) $R(A_H)$; (**f**) $R(A_H, Z_{DR})$. Ten meteorological stations are marked with "+".

Table 1. Evaluation scores of the 3-h rainfall estimates from the CPOL radar.

Scores	Radar QPE Estimators					
	$R(Z_H)$	$R(Z_H, Z_{DR})$	$R(K_{DP})$	$R(K_{DP}, Z_{DR})$	$R(A_H)$	$R(A_H, Z_{DR})$
E_{RMS} (mm)	5.640	4.067	5.77	8.396	6.004	5.197
E_{NM}	–11.974	–8.577	12.45	21.58	16.088	–4.398
E_{CC}	0.979	0.983	0.981	0.976	0.978	0.976

$R(A_H)$ performed worse than $R(K_{DP})$ based on all evaluation scores. Although A_H was also not sensitive to the negative effects on Z_H (see Section 1), the calculation of A_H in Equation (1a) includes Φ_{DP} and the original radar measured Z_H, and A_H was less associated with rainfall rate than K_{DP}. $R(A_H)$ was also inferior to $R(Z_H)$ according to the E_{RMS} and E_{CC} scores; however, according to the E_{NM} scores shown in Table 1 and the scattergrams shown in Figure 4a,c, $R(A_H)$ tended to overestimate, especially at higher rainfall rates; in contrast, $R(Z_H)$ tended to underestimate in similar patterns. For convenience, radar-observed K_{DP} vs. Z_H and A_H vs. Z_H, shown in Figure 6b,c, respectively, can be compared to see the differences between K_{DP} and A_H. For the same Z_H values, radar-observed K_{DP} vs. Z_H shows less difference (about ±0.5 deg·km^{-1}) from T-matrix-derived K_{DP} vs. Z_H in Figure 6b. In contrast, radar-observed A_H vs. Z_H suffers from a relatively wider distribution difference (about ±0.3 dB·km^{-1} and more positive deviation with Z_H > 40 dBZ) from T-matrix-derived A_H vs. Z_H in Figure 6c. That is, radar-observed A_H seemed to be overestimated more than K_{DP} in some radar beams. An unobserved microphysical transition may occur during the falling process of the hydrometeors from the altitude of 1.6–2 km to the surface, then caused the large difference between radar-observed A_H and its surface counterparts.

In addition, $R(A_H, Z_{DR})$ performed best of the six radar QPE estimators with respect to the E_{NM} and E_{RMS} scores shown in Table 1. Essentially, it is not straightforward to resolve the performance differences between $R(K_{DP}, Z_{DR})$ and $R(A_H, Z_{DR})$, since A_H and K_{DP} have similar characteristics. They are often related through $A_H = \alpha K_{DP}$. Therefore, we aimed to decompose their mathematical formulas into two parts (see Figure 9). In particular, $R(K_{DP}, Z_{DR})$ consists of K_{DP}- and Z_{DR}-related components, whereas $R(A_H, Z_{DR})$ consists of A_H- and Z_{DR}-related components. Since the K_{DP}- and A_H-related calculations behave similarly (see Figure 9a,b), the Z_{DR}-related components play a dominant role in the differences. We noticed that $R(K_{DP}, Z_{DR})$ is more associated with overestimation compared with $R(A_H, Z_{DR})$, and the Z_{DR}-related calculation in $R(A_H, Z_{DR})$ decreases more quickly than that of $R(K_{DP}, Z_{DR})$ (see Figure 9c). All in all, the differences between $R(K_{DP}, Z_{DR})$ and $R(A_H, Z_{DR})$ are more related to the Z_{DR}-related component. Besides, Figure 8f shows that many scatter dots were distributed below the diagonal line when gauge measurements were less than 10 mm, and these underestimates may partly compromise the overestimates when the 3-h gauge measurements exceeded 75 mm, which was an important reason for the superior scores of $R(A_H, Z_{DR})$.

The comparison between different radar QPE approaches showed that $R(K_{DP})$ performs best of all the single-parameter radar QPE estimators in the range 0–75mm, and $R(A_H, Z_{DR})$ performs best with respect to E_{NM} scores. However, this result cannot be declared just based on the statistical scores. Not all polarimetric radar QPE estimators, such as $R(K_{DP}, Z_{DR})$, can obtain superior statistical scores to $R(Z_H)$. Instead, the detailed scatter distributions in Figure 8c–f show that $R(K_{DP})$, $R(K_{DP}, Z_{DR})$, $R(A_H)$, and $R(A_H, Z_{DR})$ were all overestimated when gauge measurements exceeded 50 mm. This indicates that manually alternating polarimetric radar variables cannot always obtain better performances. The rainfall center area is worthy of further investigation to reveal some negative factors, which seriously affect the practical performance of these polarimetric radar QPE algorithms.

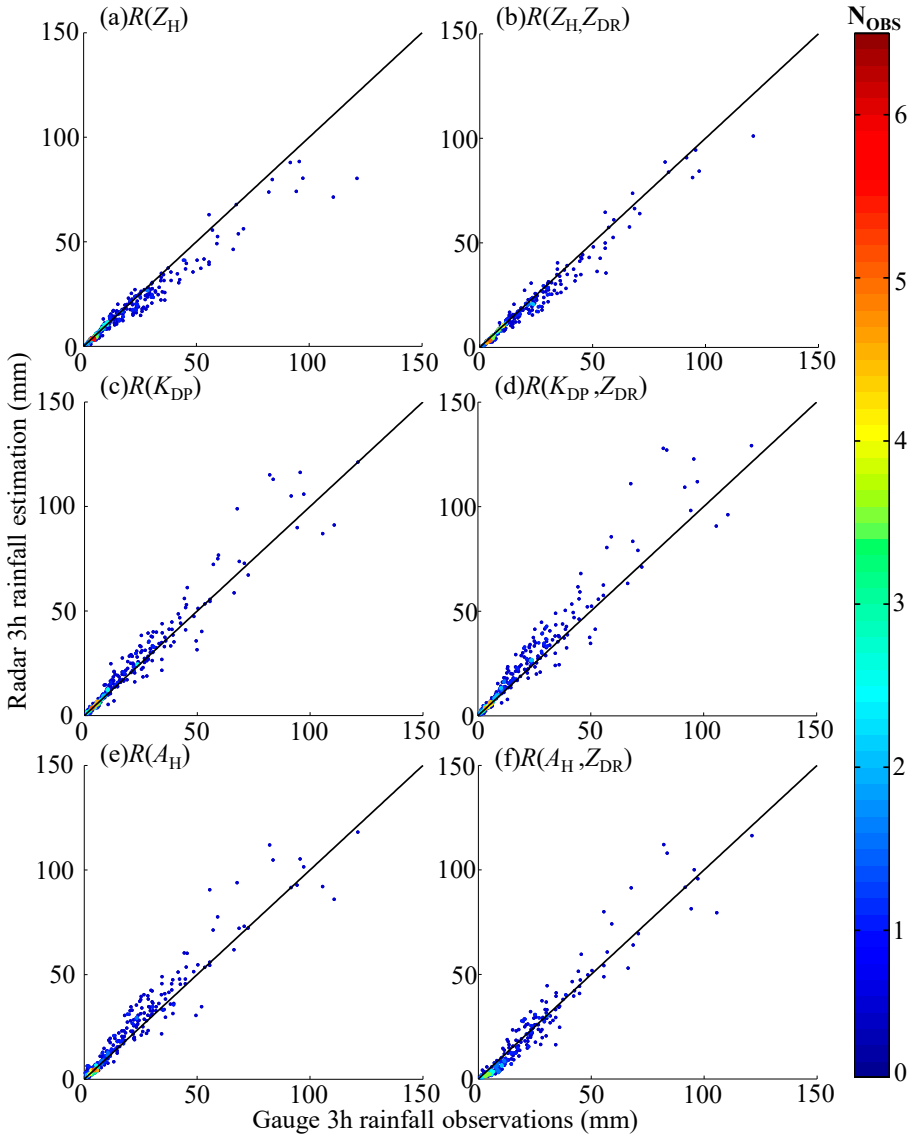

Figure 8. Scattergram of 3-h rainfall estimates from the gauge versus radar using six different radar rainfall estimators at 0500 UTC on 1 June 2016: (**a**) $R(Z_H)$; (**b**) $R(Z_H, Z_{DR})$; (**c**) $R(K_{DP})$; (**d**) $R(K_{DP},Z_{DR})$; (**e**) $R(A_H)$; (**f**) $R(A_H, Z_{DR})$.

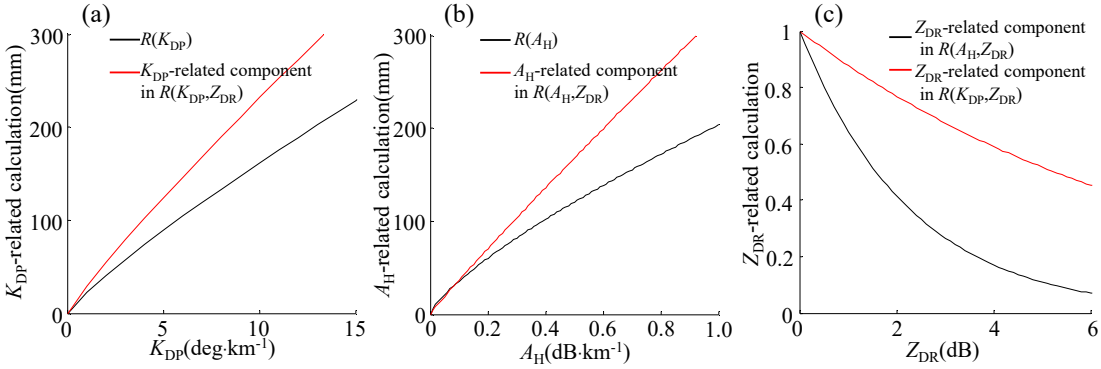

Figure 9. Different radar variable related components: (**a**) K_{DP}-related component; (**b**)A_H-related component; (**c**)Z_{DR}-related component.

3.4. Time Series Analysis

Gauge-measured, DSD-based, and radar-estimated hourly rainfall time series from ten meteorological stations, which are located within the rainfall center area shown in Figure 7, are shown in Figure 10. Although only CA and JD stations were used to observe the DSD dataset, the near agreement of DSD-based and gauge-measured hourly rainfall (bold black and green lines) shown in Figure 10a,b verifies the high quality of these gauge measurements; therefore, the gauge-measured rainfall time series of the other eight stations can also provide good surface reference rainfall for radar estimates too. Moreover, some typical error characteristics related to different radar rainfall patterns can be directly reflected through these temporal rainfall series.

Figure 10a shows a good positive example that nearly all radar-estimated rainfall series at CA station were in good accordance with the gauge-measured rainfall series with an exception of $R(Z_H)$, which was underestimated at 0200–0400 UTC. The time series at QDH at 0200–0500 UTC shown in Figure 10c and that at GX at 0300–0500 UTC shown in Figure 10d were very similar to those shown in Figure 10a. They can be assumed to have similar rainfall patterns. Although the optimum rainfall retrieval relationship is necessary for a good rainfall estimator, the small deviation between the radar-estimated rainfall series of $R(A_H)$, $R(K_{DP})$, $R(Z_H, Z_{DR})$, $R(A_H, Z_{DR})$ and the gauge-measured rainfall series in Figure 10a can also be attributed to the consistency between the radar-observed series of Z_H, Z_{DR}, $K_{DP,}$ and A_H and their T-matrix-derived counterparts in Figure 11a,c,e,g. Furthermore, most radar-observed and T-matrix-derived ρ_{HV} values exceed 0.99 in Figure 11i, which indicates that radar observed pure liquid hydrometeors up in the air are similar to those near the surface. Accordingly, the ellipses depicted in Figure 11c,d implies that the overestimated K_{DP} and A_H values observed by radar can account for their overestimated rainfall near 0200 UTC in Figure 10a too. On the contrary, the large deviation of $R(Z_H)$ from the gauge rainfall series can be attributed to the inadequate $R(Z_H)$ relationship, as described in Section 3.3.

The overestimation of the time series of $R(A_H)$, $R(K_{DP})$, $R(K_{DP}, Z_{DR})$, $R(A_H, Z_{DR})$ at JD station at 0300–0400 UTC (Figure 10b), at ZY station at 0400–0500 UTC (Figure 10h), at GL station at 0300–0500 UTC (Figure 10i), and at JZL station at 0340–0440 UTC feature similar rainfall patterns. In contrast, the rainfall series estimated by $R(Z_H)$ and $R(Z_H, Z_{DR})$ agreed well with the gauge rainfall series in these time intervals. Some characteristics can be deduced from the data timeseries of JD station in Figure 12. The difference of ρ_{HV} depicted in Figure 12e indicates the hydrometeors in the radar beams and near the surface were microphysically different, namely, some solid hydrometeors may exist in the upper air, but only liquid hydrometeors fell on the surface. Thus, there existed an unobserved microphysical transition before the solid hydrometeors falling on the ground. The large Z_{DR} values near the surface in Figure 12b corresponded to big raindrops at the start of the showers; however, radar-observed Z_{DR} values were all less than 2 dB during this period, which indicates the diameter of the hydrometeors in the air were still smaller than 2 mm and the Mie scattering effects were not obvious in some radar volumes. Therefore, radar-observed K_{DP} and A_H in Figure 12c,d may be overestimated than expected if the contribution of the solid hydrometeors was not separated successfully from Φ_{DP}. The reason for the small biases between radar-observed Z_H and surface-T-matrix-derived Z_H in Figure 12a can be ascribed to the fact that a large raindrop can account for a large number of little raindrops, namely, more large raindrops were observed near the surface than in the upper air, which had been verified by the large bias of Z_{DR}. Consequently, radar-observed Z_H and T-matrix-derived Z_H might coincidently agree with each other and $R(Z_H)$ did not deviate far from the gauge-measured/DSD-based hourly rainfall series during this time period. Simultaneously, the Z_{DR}-related calculations hardly reduced the overestimation caused by the A_H-related or K_{DP}-related calculations of $R(A_H, Z_{DR})$ and $R(K_{DP}, Z_{DR})$ during the same period. Instead, $R(Z_H, Z_{DR})$ outperformed the other five radar QPE estimators and its rainfall time series was most similar to the gauge-measured and DSD-based hourly rainfall series of JD station.

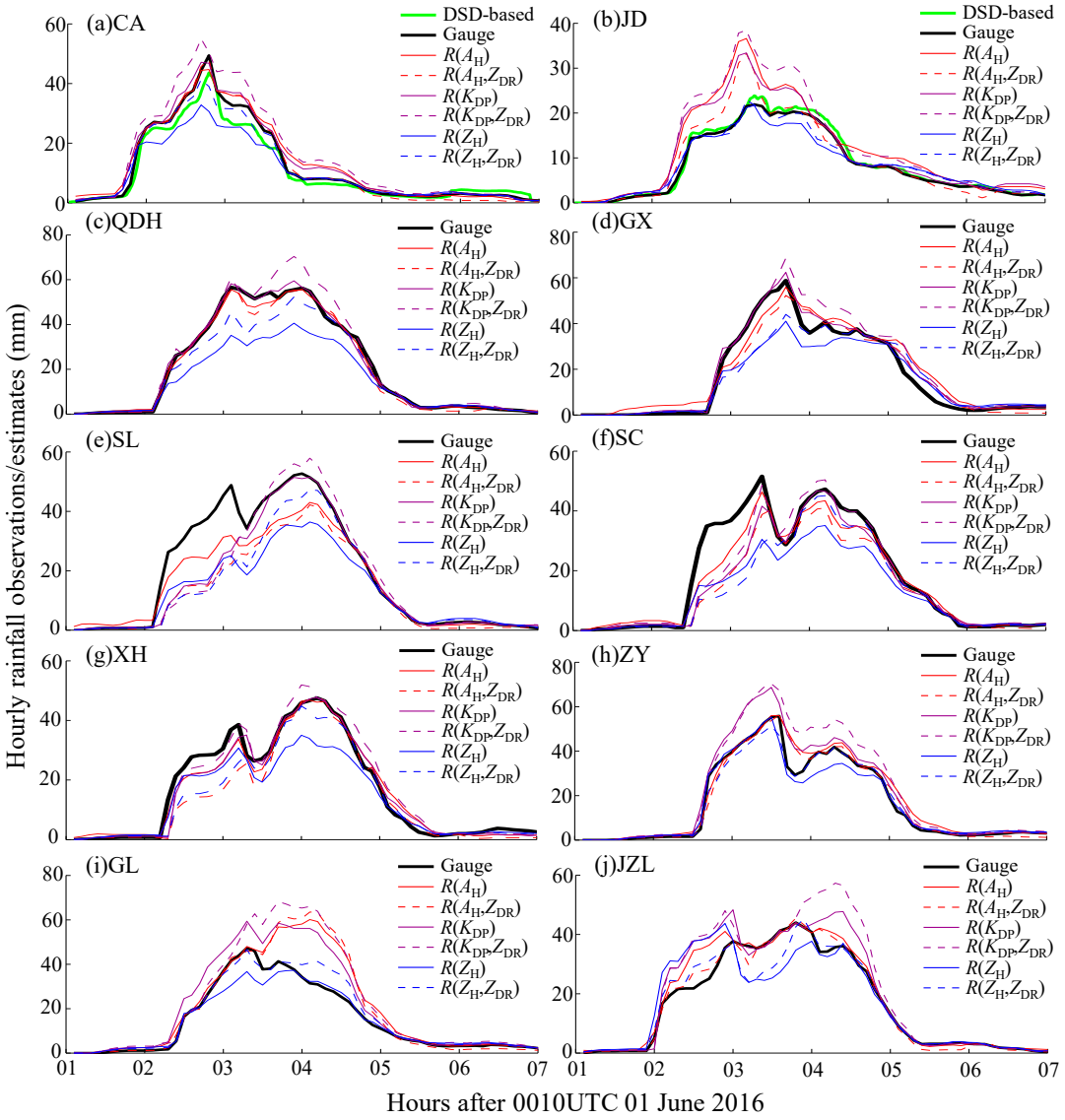

Figure 10. Time series of hourly rainfall estimates for 60 minute moving windows from the 10 gauges, disdrometer and radar between 0100–0700 UTC on 1 June 2016: (**a**) CA, (**b**) JD, (**c**) QDH, (**d**) GX, (**e**) SL, (**f**) SC, (**g**) XH, (**h**) ZY, (**e**) GL and (**j**) JZL.

The time series of all radar estimates at SL and SC stations were all underestimated at 0200–0330, as shown in Figure 10e,f. The rainstorm system, which was featured abundant moisture (see Figure 5), moved along the northwest direction and successively affected SL, XH, and SC stations. These radar rainfall underestimations were caused by showers at the start of the major rainstorm. The detailed information of Z_H, Z_{DR}, and K_{DP}, as well as the six-minute rainfall measurements at these three stations are all listed in Table 2, where the radar captured only one peak value each of Z_H, Z_{DR}, and K_{DP} at SL and SC stations. However, the CPOL radar captured two peak values each of Z_H, Z_{DR}, and K_{DP} at XH station. Through comparing the six-minute rainfall recordings from the gauges, SL, XH, and SC were found to have two peak values of Z_H, Z_{DR}, and K_{DP} each. That is, the CPOL radar failed to detect the second peak values of Z_H, Z_{DR}, and K_{DP} at SL and SC stations due to the rapid development and movement of the shower in front of the rainstorm. As a result, all radar estimates at SL and SC tended to underestimate the hourly rainfall accumulations, and this underestimation lasted for about one hour.

Table 2. Radar measurements and six-minute gauge rainfall measurements of the three stations during 0212–0330 UTC on 1 June 2016. The bold font marks first two timeframes of the shower at each station.

Time (UTC)	Z_H (dBZ)			Z_{DR} (dB)			K_{DP} (deg·km^{-1})			Gauge Rainfall (mm)		
	SL	XH	SC	SL	XH	SC	SL	XH	SC	SL	XH	SC
0212	**53.6**	-	-	**2.06**	-	-	**4.50**	-	-	**13.7**	0.0	0.0
0218	**16.5**	**51.8**	-	**0.1**	**2.05**	-	**0.0**	**6.89**	-	**11.9**	**12.7**	0.0
0224	40.9	**50.8**	-	1.19	**2.90**	-	1.19	**3.24**	-	1.7	**8.2**	0.1
0230	11.3	35.2	**54.4**	0.6	0.87	**1.85**	0.20	0.41	**5.88**	3.2	2.9	**14.3**
0236	22.9	16.7	**15.9**	0.02	0.03	**1.78**	0.04	-	**0.733**	3.9	3.9	**12.7**
0242	27.3	22.1	20.1	0.46	0.07	0.21	0.00	0.06	0.01	1.1	0.6	7.5
0248	28.5	36.5	39.1	0.25	0.73	1.43	0.03	0.02	0.75	1.7	0.1	1.1
0254	49.9	43.8	29.4	1.97	1.39	0.33	2.95	0.46	0.34	3.2	0.2	0.1
0300	40.5	44.7	44.7	0.85	1.23	1.21	0.35	0.73	1.23	4.6	1.9	0.9
0306	33.5	45.4	31.7	0.49	1.07	0.53	0.26	1.70	0.09	3.8	6.3	2.7
0312	47.4	43.7	46.8	1.39	1.05	1.44	2.96	0.72	1.90	4.4	1.8	3.6
0318	44.9	40.6	48.5	0.69	0.94	1.07	1.26	0.89	3.54	6.6	2.3	4.1
0324	47.9	39.8	47.7	1.26	0.72	1.15	2.27	0.47	0.88	7.1	6.4	4.6
0330	49.2	45.7	33.8	1.03	0.96	0.37	2.51	1.32	0.36	7.0	3.6	3.0

Figure 10h demonstrates another typical pattern where $R(A_H)$ and $R(A_H, Z_{DR})$ were both superior to $R(K_{DP})$ and $R(K_{DP}, Z_{DR})$ and the latter two were both overestimated at 0230–0500 UTC. Since the optimal rainfall retrieval relationships were used, the performance difference was mainly attributed to the different characteristics of A_H and K_{DP}. A_H is often estimated through $A_H = \alpha K_{DP}$. In addition, the reconstructed Φ_{DP} calculated through the fitting process (K_{DP} fitting) or ZPHI processing (A_H) should both be similar to the filtered Φ_{DP}. Hence, it can be concluded that the major difference between A_H and K_{DP} is in the coefficient α, which is adjustable in $[r_0, r_m]$. Moreover, for the same $\Delta\Phi_{DP}$ (r_0, r_m), it is well known that the difference in Z_H^M will not affect the A_H because A_H is also immune to attenuation, miscalibration, PBB, and wet radome issues. Based on Equation (1a), coefficient α must be different in the process in order to maintain such a statement. In the pure liquid rain scenario, both K_{DP} and A_H were expected to increase as the attenuation corrected Z_H increased. For the mixed phase hydrometeors in the melting layer, both K_{DP} and A_H tended to be near-zero if $\Delta\Phi_{DP}$ (r_0, r_m) could be constrained by a small value during the estimation process; otherwise, they might be overestimated if $\Delta\Phi_{DP}$ (r_0, r_m) was large, which is similar to the pure rain scenario.

Furthermore, due to the changes in coefficient α, the consistency between A_H and Z_H is not as strong as that between K_{DP} and Z_H and/or Z_{DR} (for details on the self-consistency of polarimetric radar measurements, see [39]). To further support such a conclusion, Figure 6 shows that the radar-observed K_{DP} vs. Z_H (Figure 6b) measurements are consistent with the T-matrix-derived scattergram of K_{DP} vs. Z_H. However, the radar-observed scattergram of A_H vs. Z_H (Figure 6c) is not as consistent. Instead, there is an obvious divergence when Z_H exceeds 40 dBZ, which is more obvious than that of K_{DP} vs. Z_H in Figure 6b. Such divergence is further investigated using Figure 6c, which led to the separation of the radar-observed scattergram of A_H vs. Z_H into three categories:

(i) Radar-observed data overlap with the T-matrix-derived data: Radar-observed A_H values within the range gates are nearly the same as T-matrix-derived A_H. Using the optimal $R(A_H)$ relationships, unbiased $R(A_H)$ is expected compared with the R calculated directly from DSD and surface gauge rainfall measurements (see Figure 4e).

(ii) Radar-observed data above the T-matrix-derived data: These radar-observed A_H values are potentially higher than the ideal observations near the surface, which is caused by the contamination of some small-sized melting hydrometeors with the diameter less than 2 mm. These radar-observed A_H values may further cause the overestimation of $R(A_H)$ if radar-observed A_H values are directly applied (Figure 4e). Due to the narrow range of A_H, a little deviation may introduce a large difference in $R(A_H)$. As such, a correction procedure for A_H may be required.

(iii) Radar-observed data below the T-matrix-derived data: This is dominated by the near-zero A_H values, and their range gates are more associated with the melting mixed phase hydrometers. Although Z_H^M can be large in $[r_0, r_m]$, $\Delta\Phi_{DP}$ (r_0, r_m) may be small in Equation (1a) due to the non-negative constraint imposed on A_H estimation, the coefficient α can adjust the non-Z_H^M part of Equation (1a), resulting in reconstructed Φ_{DP} close to the filtered Φ_{DP}.

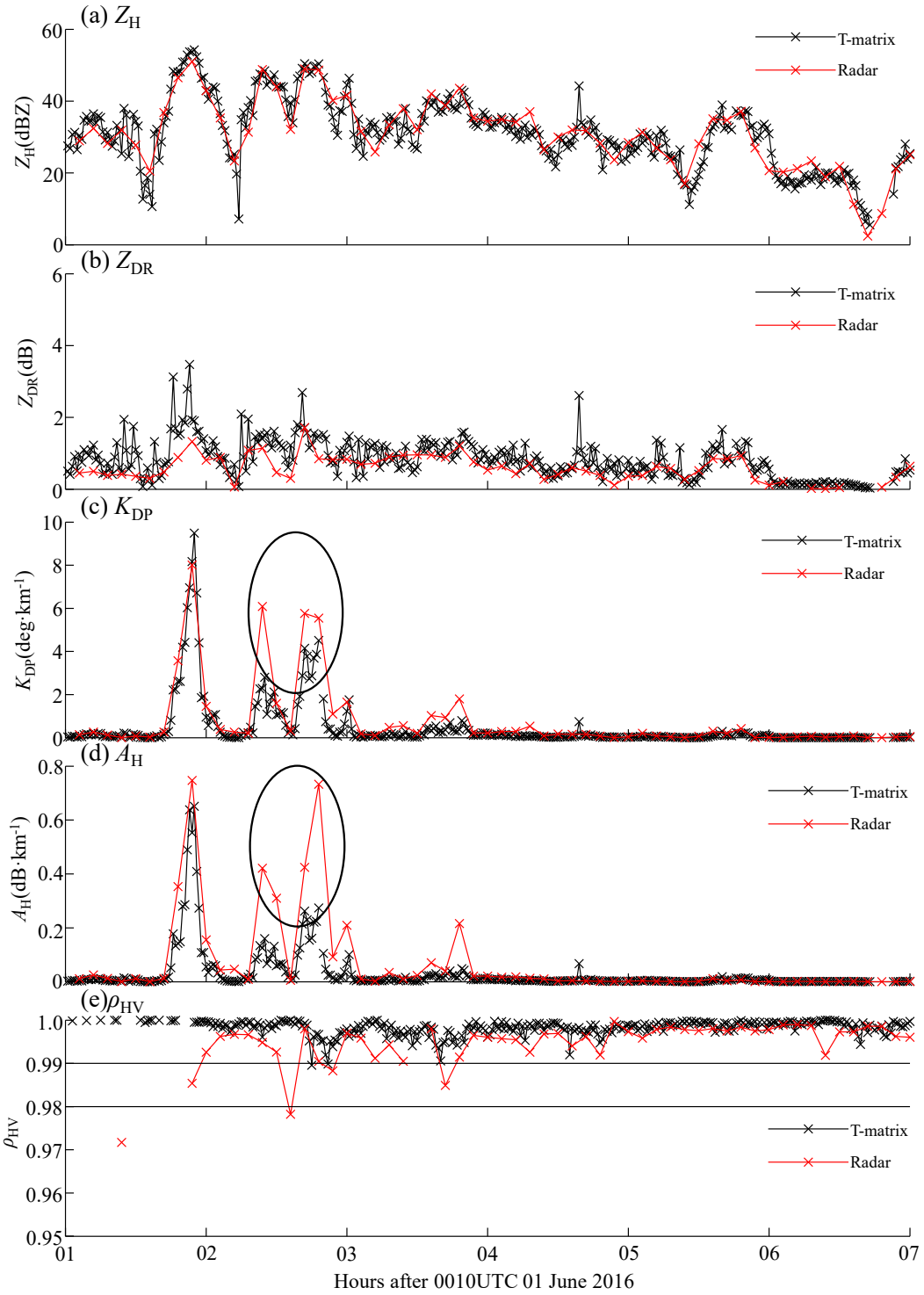

Figure 11. T-matrix-derived radar variables and CPOL radar measurements at CA station at 0100–0700 UTC on 1 June 2016: (**a**) Z_H, (**b**) Z_{DR}, (**c**) K_{DP}, (**d**) A_H, and (**e**) ρ_{HV}. The ellipses on (c) and (d) indicate that the radar-observed K_{DP} and A_H values are larger than the T-matrix-simulated ones.

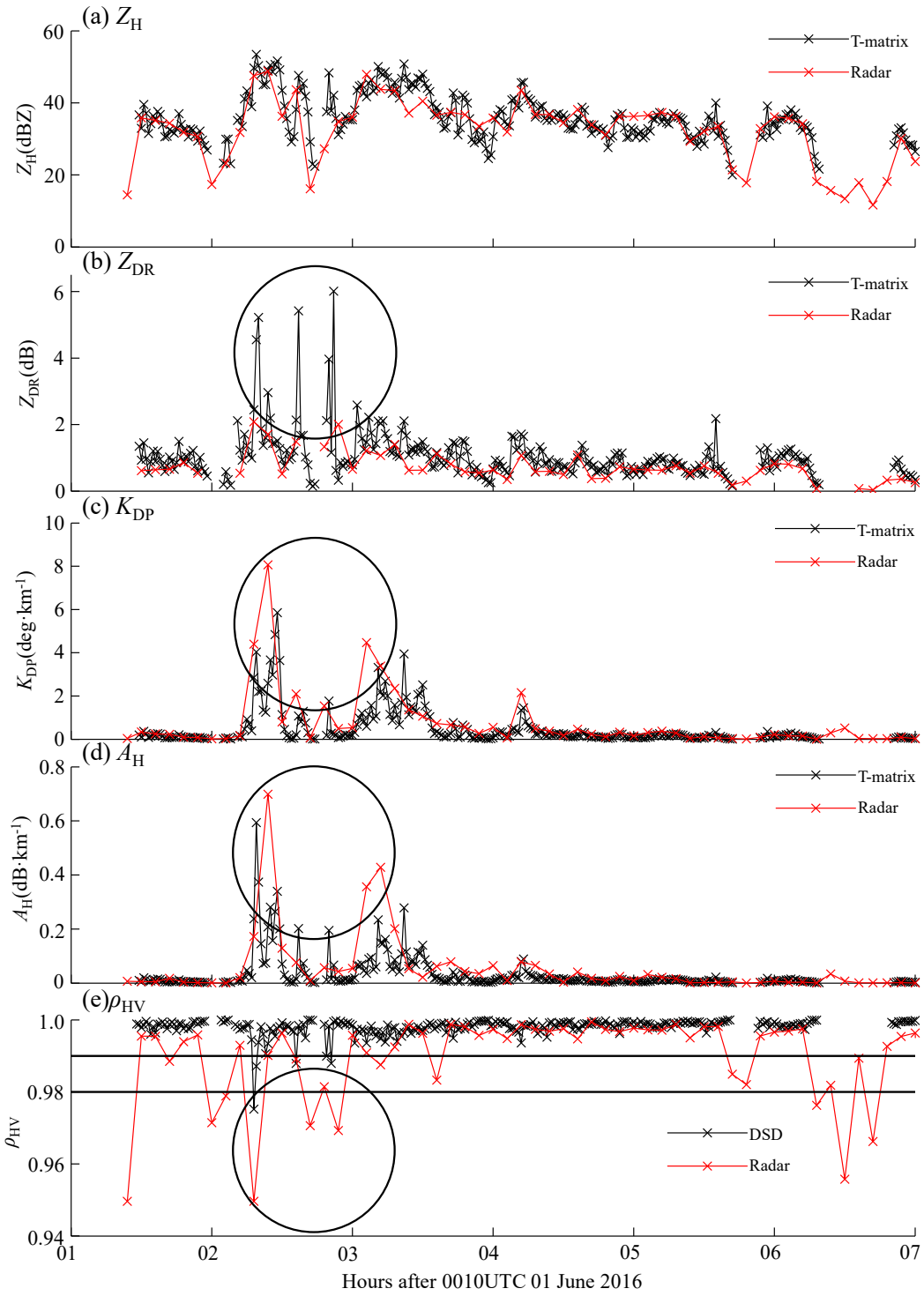

Figure 12. T-matrix-derived radar variables and CPOL radar measurements at JD station at 0100–0700 UTC on 1 June 2016: (**a**) Z_H, (**b**) Z_{DR}, (**c**) K_{DP}, (**d**) A_H, and (**e**) ρ_{HV}. The ellipses on (b–e) indicate larger radar-observed K_{DP} and A_H values but smaller Z_{DR} and ρ_{HV} values than T-matrix-derived ones.

3.5. Discussion

The statistical comparison in Section 3.3 actually gives an overall view of the error characteristics of these radar QPE estimators. More error information about each radar QPE estimator can be seen by comparing the time series of radar rainfall estimates with gauge rainfall measurements. This shows that the optimum rainfall rate relationships and the consistency between radar measurements and

their surface counterparts are both indispensable, and the relative superiority of polarimetric radar QPE estimators is closely related to the specific rainfall patterns. The following should be noted:

(i) Regionally optimal rainfall estimation relationships are the basis for radar QPE. The C-band relations for $R(Z_H)$, $R(A_H)$, and $R(K_{DP})$ provided in this paper are significantly different from those given in [23,40,41]. Similar comparable results may be not expected if the same equation parameters are directly implemented for severe rainfall events in this paper, because they may be representative of different localized precipitation characteristics, which intrinsically varies around the world. This is the reason why individual equations of $R(Z_H)$, $R(A_H)$, and $R(K_{DP})$ are always necessary for different locations; (ii) $R(Z_H)$ is not always an optimal option for polarimetric radar. However, it was observed that $R(Z_H)$ is not always inferior to other rainfall estimators, and $R(Z_H)$ really performed best at 0100–0310 UTC (Figure 10b) and at 0100–0340 UTC (Figure 10h), where the time series of $R(Z_H)$ tended to overlap with the gauge time series in these specific temporal intervals. Besides, the overestimation effects caused by the melting layers on $R(Z_H)$ can be solved by some bright band identification procedure, and more adequate $R(Z_H)$ relationships suitable for severe rainfall scenario or self-adaptive $R(Z_H)$ relationships may further enhance the performance of $R(Z_H)$. Therefore, Z_H is still useful for the range gates where K_{DP} or A_H is abnormally higher.

(iii) In this paper, $R(Z_H, Z_{DR})$ is a positive example of Z_{DR} utilization and it performs better than $R(Z_H)$ in many of the time series depicted in Figure 10. Comparing the mathematical forms of $R(Z_H)$ and $R(Z_H, Z_{DR})$, the integration with Z_{DR} really mitigates some underestimation of $R(Z_H)$. In contrast, $R(K_{DP}, Z_{DR})$ presented more overestimates than $R(K_{DP})$, which implies that integrating Z_{DR} with K_{DP} through current mathematical form may not be effective. In addition, although $R(A_H, Z_{DR})$ obtained the best E_{NM} scores, it underestimated in light rainfall scenarios more seriously than $R(A_H)$. Some regional correction upon the rainfall field derived from $R(K_{DP}, Z_{DR})$ and $R(A_H, Z_{DR})$ may be necessary to improve their performance.

(iv) The melting layer not only causes the overestimation of $R(Z_H)$ but can also introduce overestimation to $R(A_H)$ and $R(K_{DP})$. If radar-observed K_{DP} or A_H were contaminated by the melting layer but the hydrometeors near the surface were not, $R(K_{DP})$ and $R(A_H)$ might be overestimated. Although the α coefficient can adjust to mitigate some bias of $R(A_H)$, which helps it to outperform $R(K_{DP})$, the overestimation related to $R(A_H)$ remains serious. Some correction procedures aiming to make radar-observed A_H or K_{DP} more approximate to the counterparts of surface hydrometers have shown promise for future use; however, some statistical prior knowledge on the regional rainfall characteristics may be necessary during this process.

(v) The convective rainstorms with a quick moving speed may cause all radar QPE estimators to be underestimated if the radar failed to capture the full view of the rainstorm. Such rainfall patterns correspond to the initial developing phase of the rainstorms. The low-cost gap-filling X-band radar network may help to instantly observe such rainstorms in their initial developing phase. The phased array radar supporting quick VCP scanning strategy also helps to provide high temporal resolution dataset for such rainstorms. Both are promising to make the monitoring of rainstorms more spatiotemporally seamless for radar QPE retrievals.

Dynamic composition of the different radar QPE estimators is a promising trend, and all of the different radar rainfall estimators can be comprehensively utilized in this way. However, the optimal and representative relationships incorporating a variety of rainfall characteristics over a target area, the high-quality radar measurements similar to the counterparts of surface hydrometeors, and the detailed composition forms of these radar QPE estimators are all important factors that make the ultimate rainfall estimation results efficient in practical operations. None of the abovementioned issues can be neglected during this process and they are worthy of further investigation in the future.

4. Summary

Efficient utilization of the polarimetric radar variables to estimate rainfall is critical for timely severe rainfall warnings and subsequent hydrometeorological applications. Polarimetric radar has provided

many possible combinations of different QPE estimators. This paper evaluated the performance of three single-parameter and three double-parameter-based radar QPE relations using CPOL radar measurements during a severe waterlogging event in eastern China. The evaluation scores, scattergrams and the rainfall time series within the rainfall field center were compared in details. The main findings are summarized as follows:

(i) $R(A_H, Z_{DR})$ performed the best among the six QPE estimators in this waterlogging event according to the E_{NM} score, although it introduced underestimation in light rain areas. The incorporation of Z_{DR} improved the performance of both $R(Z_H, Z_{DR})$ and $R(A_H, Z_{DR})$ over their single- parameter counterparts, but the improvement was negligible in $R(K_{DP}, Z_{DR})$ during this particular event. The basic calculation form of the Z_{DR}-related component in $R(K_{DP}, Z_{DR})$ may be responsible for this phenomenon.

(ii) In addition to the optimal rainfall relationship, the consistency between radar measurements aloft and their surface counterparts was also necessary for accurate rainfall estimation near ground level. The contamination of melting solid hydrometeors on A_H and K_{DP} can make $R(A_H)$, $R(A_H, Z_{DR})$, $R(K_{DP})$, and $R(K_{DP}, Z_{DR})$ less effective than $R(Z_H)$ and $R(Z_H,Z_{DR})$. In addition, the adjustment of the α coefficient for estimating A_H can partly reduce some of the impact of melting hydrometeors and thus improve the performance of the A_H–based rainfall estimator.

(iii) The practical performance and relative advantages of different radar QPE estimators are seriously affected by different rainfall patterns. On the one hand, all radar QPE estimators tend to underestimate rainfall if the radar failed to capture the rapid evolvement of the rainstorms. On the other hand, each radar QPE estimator can outperform others during some time intervals with particular rainfall characteristics.

In summary, utilizing polarimetric techniques to improve radar QPE is not as simple as just replacing radar variables in the radar rainfall relations. Instead, the identification of different rainfall characteristics and the implementation of optimal or adaptive rainfall algorithms are critical for obtaining accurate QPE data. In addition, the use of high-resolution gap-filling X-band radar networks (e.g., [42]) or phased array radars is a promising way to further enhance the radar-derived rainfall product.

Author Contributions: Y.G. carried out the data collection and detailed analysis. Y.G. was also involved in the development of the polarimetric radar data processing and product generation systems. H.C. and J.Z. supervised the work and provided critical comments. J.Z. conducted the detailed literature review. Y.G. and H.C. prepared the first draft of this manuscript. J.Z. reviewed and edited the manuscript.

Funding: This research was primarily supported by the National Natural Science Foundation of China (NSFC) under grant 41705018 and the Zhejiang Provincial Natural Science Fund through award LY17D050001.

Acknowledgments: The C-band polarimetric radar and gauge data were provided by the Hangzhou Meteorological Bureau (HMB). The authors would like to thank the forecasters at HMB for the discussion of this severe weather event. Thanks to the anonymous reviewers for their great comments that helped us improve this manuscript.

Conflicts of Interest: The authors declare no conflicts of interest.

References

1. Bringi, V.N.; Rico-Ramirez, M.A.; Thurai, M. Rainfall Estimation with An Operational Polarimetric C-Band Radar in the United Kingdom: Comparison with A Gauge Network and Error Analysis. *J. Hydrometeorol.* **2010**, *12*, 935–954. [CrossRef]
2. Chandrasekar, V.; Wang, Y.; Chen, H. The CASA Quantitative Precipitation Estimation System: A Five-Year Validation Study. *Nat. Hazards Earth Syst. Sci.* **2012**, *12*, 2811–2820. [CrossRef]
3. Chandrasekar, V.; Chen, H.; Philips, B. Principles of high-resolution radar network for hazard mitigation and disaster management in an urban environment. *J. Meteorol. Soc. Jpn.* **2018**, *96A*, 119–139. [CrossRef]
4. Cifelli, R.; Chandrasekar, V.; Chen, H.; Johnson, L.E. High Resolution Radar Quantitative Precipitation Estimation in the San Francisco Bay Area: Rainfall Monitoring for the Urban Environment. *J. Meteorol. Soc. Jpn.* **2018**, *96A*, 141–155. [CrossRef]

5. Chen, H.; Lim, S.; Chandrasekar, V.; Jang, B.-J. Urban Hydrological Applications of Dual-Polarization X-Band Radar: Case Study in Korea. *J. Hydrol. Eng.* **2017**, *22*, E5016001. [CrossRef]
6. Chen, H.; Chandrasekar, V.; Bechini, R. An Improved Dual-Polarization Radar Rainfall Algorithm (DROPS2.0): Application in NASA IFloodS Field Campaign. *J. Hydrometeorol.* **2017**, *18*, 917–937. [CrossRef]
7. Chen, H.; Chandrasekar, V. Estimation of Light Rainfall using Ku-band Dual-Polarization Radar. *IEEE Trans. Geosci. Remote Sens.* **2015**, *53*, 5197–5208. [CrossRef]
8. Krajewski, W.F.; Smith, J.A. Radar hydrology: Rainfall estimation. *Adv. Water Resour.* **2002**, *25*, 1387–1394. [CrossRef]
9. Gebremichael, M.; Testik, F.Y. Microphysics, measurement, and analyses of rainfall. *Rainfall State Sci. Geophys. Monogr.* **2013**, *191*, 1–6.
10. Dance, S.L.; Ballard, S.P.; Bannister, R.N.; Clark, P.; Cloke, H.L.; Darlington, T.; Flack, D.L.A.; Gray, S.L.; Hawkness-Smith, L.; Husnoo, N.; et al. Improvements in Forecasting Intense Rainfall: Results from the FRANC (Forecasting Rainfall Exploiting New Data Assimilation Techniques and Novel Observations of Convection) Project. *Atmosphere* **2019**, *10*, 125. [CrossRef]
11. Krajewski, W.F.; Villarini, G.; Smith, J.A. Radar-Rainfall Uncertainties. *Bull. Am. Meteorol. Soc.* **2010**, *91*, 87–94. [CrossRef]
12. Zhang, J.; Howard, K.; Langston, C.; Kaney, B.; Qi, Y.; Tang, L.; Grams, H.; Wang, Y.; Cocks, S.; Martinaitis, S.; et al. Multi-Radar Multi-Sensor (MRMS) Quantitative Precipitation Estimation: Initial Operating Capabilities. *Bull. Am. Meteorol. Soc.* **2016**, *97*, 621–638. [CrossRef]
13. Gou, Y.; Ma, Y.; Chen, H.; Wen, Y. Radar-derived Quantitative Precipitation Estimation in Complex Terrain over The Eastern Tibetan Plateau. *Atmos. Res.* **2018**, *203*, 286–297. [CrossRef]
14. Frasier, S.; Kabeche, F.; Ventura, J.F.I.; Al-Sakka, H.; Bousquet, O. In-situ estimation of wet-radome attenuation at x-band. *J. Atmos. Ocean. Technol.* **2013**, *30*, 917. [CrossRef]
15. Matrosov, S.Y. Evaluating polarimetric X-band radar rainfall estimators during HMT. *J. Atmos. Ocean. Technol.* **2010**, *27*, 122–134. [CrossRef]
16. Park, S.G.; Maki, M.; Iwanami, K.; Bringi, V.N.; Chandrasekar, V. Correction of Radar Reflectivity and Differential Reflectivity for Rain Attenuation at X Band. Part II: Evaluation and Application. *J. Atmos. Ocean. Technol.* **2005**, *22*, 1633–1655. [CrossRef]
17. Sachidananda, M.; Zrnic, D.S. Differential propagation phase shift and rainfall rate estimation. *Radio Sci.* **1986**, *21*, 235–247. [CrossRef]
18. Ryzhkov, A.V.; Giangrande, S.E.; Schuur, T.J. Rainfall Estimation with A Polarimetric Prototype of WSR-88D. *J. Appl. Meteorol.* **2005**, *44*, 502–515. [CrossRef]
19. Gosset, M.; Zahiri, E.P.; Moumouni, S. Rain Drop Size Distribution Variability and Impact on X-band Polarimetric Radar Retrieval: Results from the AMMA Campaign in Benin. *Q. J. R. Meteorol. Soc.* **2010**, *136*, 243–256. [CrossRef]
20. Schneebeli, M.; Bern, A. An extended Kalman Filter Framework for Polarimetric X-band Weather: Radar Data Processing. *J. Atmos. Ocean. Technol.* **2012**, *29*, 711–730. [CrossRef]
21. Anagnostou, E.N.; Anagnostou, M.N.; Krajewski, W.F.; Kruger, A.; Miriovsky, B.J. High-resolution rainfall estimation from X-band polarimetric radar measurements. *J. Hydrometeorol.* **2004**, *5*, 110–128. [CrossRef]
22. Matrosov, S.Y.; Clark, K.A.; Martner, B.E.; Tokay, A. X-band polarimetric radar measurements of rainfall. *J. Appl. Meteorol.* **2002**, *41*, 941–952. [CrossRef]
23. Ryzhkov, A.V.; Diederich, M.; Zhang, P.; Simmer, C. Potential Utilization of Specific Attenuation for Rainfall Estimation, Mitigation of Partial Beam Blockage, and Radar Networking. *J. Atmos. Ocean. Technol.* **2014**, *31*, 599–619. [CrossRef]
24. Wang, Y.; Zhang, P.; Ryzhkov, A.V.; Zhang, J.; Chang, P. Utilization of Specific Attenuation for Tropical Rainfall Estimation in Complex Terrain. *J. Hydrometeorol.* **2014**, *15*, 2250–2266. [CrossRef]
25. Mishra, K.V.; Krajewski, W.F.; Goska, R.; Ceynar, D.; Seo, B.C.; Kruger, A.; Niemeier, J.J.; Galvez, M.B.; Thurai, M.; Bringi, V.N.; et al. Deployment and Performance Analyses of High-resolution Iowa XPOL Radar System during the NASA IFloodS Campaign. *J. Hydrometeorol.* **2016**, *17*, 455–479. [CrossRef]
26. Keenan, T.D.; Carey, L.D.; Zrnić, D.S.; May, P.T. Sensitivity of 5-cm Wavelength Polarimetric Radar Variables to Raindrop Axial Ratio and Drop Size Distribution. *J. Appl. Meteorol.* **2001**, *40*, 526–545. [CrossRef]
27. Thurai, M.; Mishra, K.V.; Bringi, V.N.; Krajewski, W.F. Initial Results of a New Composite-Weighted Algorithm for Dual-Polarized X-Band Rainfall Estimation. *J. Hydrometeorol.* **2017**, *18*, 1081–1100. [CrossRef]

28. Bringi, V.N.; Keenan, T.D.; Chandrasekar, V. Correcting C-band Radar Reflectivity and Differential Reflectivity Data for Rain Attenuation: A Self-consistent Method with Constraints. *IEEE Trans. Geosci. Remote Sens.* **2001**, *39*, 1906–1915. [CrossRef]
29. Gou, Y.; Chen, H.; Zheng, J. An Improved Self-Consistent Approach to Attenuation Correction for C-band Polarimetric Radar Measurements and Its Impact on Quantitative Precipitation Estimation. *Atmos. Res.* **2019**, *226*, 32–48. [CrossRef]
30. Gou, Y.; Ma, Y.; Chen, H.; Yin, J. Utilization of a C-band Polarimetric Radar for Severe Rainfall Event Analysis in Complex Terrain over Eastern China. *Remote Sens.* **2019**, *11*, 22. [CrossRef]
31. Hubbert, J.; Dixon, M.; Ellis, S. Weather Radar Ground Clutter. Part II: Real-Time Identification and Filtering. *J. Atmos. Ocean. Technol.* **2009**, *26*, 1181–1197. [CrossRef]
32. Steiner, M.; Smith, J. Use of three-dimensional reflectivity structure for automated detection and removal of nonprecipitating echoes in radar data. *J. Atmos. Ocean. Technol.* **2002**, *19*, 673–686. [CrossRef]
33. Wang, Y.; Chandrasekar, V. Algorithm for Estimation of The Specific Differential Phase. *J. Atmos. Ocean. Technol.* **2009**, *26*, 2565–2578. [CrossRef]
34. Hubbert, J.; Bringi, V.N.; Chandrasekar, V. Processing and Interpretation of Coherent Dual-polarized Radar Measurements. *J. Atmos. Ocean. Technol.* **1993**, *10*, 155–164. [CrossRef]
35. Hubbert, J.; Bringi, V.N. An Iterative Filtering Technique for The Analysis of Copolar Differential Phase and Dual Frequency Radar Measurements. *J. Atmos. Ocean. Technol.* **1995**, *12*, 643–648. [CrossRef]
36. Brandes, E.A.; Zhang, G.; Vivekanandan, J. Experiments in rainfall estimation with a polarimetric radar in a subtropical environment. *J. Appl. Meteorol.* **2002**, *41*, 674–685. [CrossRef]
37. Testud, S.; Oury, S.; Black, R.A.; Amayenc, P.; Dou, X. The concept of "normalized" distribution to describe raindrop spectra: A tool for cloud physics and cloud remote sensing. *J. Appl. Meteorol.* **2001**, *40*, 1118–1140. [CrossRef]
38. Bringi, V.N.; Chandrasekar, V. *Polarimetric Doppler Weather Radar: Principles and Applications*; Cambridge University Press: Cambridge, UK, 2001; 636p.
39. Scarchilli, G.; Gorgucci, V.; Chandrasekar, V.; Dobaie, A. Self-consistency of polarization diversity measurement of rainfall. *IEEE Trans. Geosci. Remote Sens.* **1996**, *34*, 22–26. [CrossRef]
40. May, P.T.; Keenan, T.D.; Zrnic, D.S.; Carey, L.D.; Rutledge, S.A. Polarimetric radar measurements of tropical rain at a 5-cm wavelength. *J. Appl. Meteorol.* **1999**, *38*, 750–765. [CrossRef]
41. Carlin, J.T.; Ryzhkov, A.V.; Snyder, J.C.; Khain, A. Hydrometeor mixing ratio retrievals for storm-scale radar data assimilation: Utility of current relations and potential benefits of polarimetry. *Mon. Weather Rev.* **2016**, *144*, 2981–3001. [CrossRef]
42. Chen, H.; Chandrasekar, V. The quantitative precipitation estimation system for Dallas–Fort Worth (DFW) urban remote sensing network. *J. Hydrol.* **2015**, *531*, 259–271. [CrossRef]